Enhanced methanol synthesis via CO hydrogenation under mild conditions: Tailoring Cu/ZnO/AlO catalysts through precursor selection for optimized Cu-ZnO interface

Chemical Engineering Journal 525 (2025) 169870

Contents lists available at ScienceDirect

Chemical Engineering Journal

journal homepage: www.elsevier.com/locate/cej

Enhanced methanol synthesis via CO_2 hydrogenation under mild conditions: Tailoring $Cu/ZnO/Al_2O_3$ catalysts through precursor selection for optimized Cu-ZnO interface interaction

Laura Chianese [a], Rosanna Viscardi [b], Claudia Bassano [b], Andrea Muscatello [c], Marco Fontana [c], Micaela Castellino [c,d], Gianluca Landi [e], Stefano Scognamiglio [e,c], Serena Esposito [c,*], Vincenzo Palma [a], Giuseppina Iervolino [a,*], Vincenzo Vaiano [a]

[a] Department of Industrial Engineering, University of Salerno, via Giovanni Paolo II 132, 84084, Fisciano, SA, Italy
[b] Casaccia Research Center, ENEA, Santa Maria di Galeria, Roma, 00123, Italy
[c] Department of Applied Science and Technology and INSTM Unit of Torino – Politecnico, Politecnico di Torino, Corso Duca degli Abruzzi 24, 10129, Torino, Italy
[d] Center for Sustainable Future Technologies, Istituto Italiano di Tecnologia, Via Livorno 60, 10144, Torino, Italy
[e] Istituto di Scienze e Tecnologie per l'Energia e la Mobilità Sostenibili, Piazzale V. Tecchio 80, 80125, Napoli, Italy

ARTICLE INFO

Keywords:
CO_2 hydrogenation
Methanol synthesis
$Cu/ZnO/Al_2O_3$ catalysts
Precursor salts effect
Cu-ZnO interface

ABSTRACT

Methanol synthesis via CO_2 hydrogenation is a promising route for sustainable chemical production, providing an alternative to fossil-based methanol. In this study, $Cu/ZnO/Al_2O_3$ (CZA) catalysts were synthesized via wet co-impregnation using different Cu and ZnO precursor salts (nitrate, acetate, and chloride) to investigate their impact on catalytic performance. Characterization by BET, XRD, Raman spectroscopy, UV–Vis DRS, TPR, XPS, FESEM, and STEM revealed significant differences in Cu dispersion, metal-support interaction, and Cu phase distribution. CO_2 hydrogenation tests were conducted over a temperature range of 180–350 °C and a pressure range of 1–7 bar to evaluate methanol selectivity and productivity. Characterization results showed that CZA_nitrate exhibited the strongest Cu/ZnO interaction and the highest Cu/ZnO interface content, evidenced by a prominent Cu^{2+}/ZnO charge transfer band in UV–Vis DRS, a lower-temperature reduction peak in TPR, and Cu species quantification at the Cu/ZnO interface via TPR. In contrast, CZA_chloride had significantly lower Cu/ZnO interface content, as confirmed by TPR peak deconvolution, and exhibited $CuAl_2O_4$ species formation (evidenced also by Raman and XRD), which hindered Cu-ZnO interactions. Among the catalysts tested, CZA_nitrate demonstrated the best catalytic performance, achieving 100 % methanol selectivity at 180–200 °C under atmospheric pressure along with the highest methanol productivity. A strong correlation between Cu/ZnO interface content and methanol productivity was further validated by linear regression analysis. Stability tests confirmed that CZA_nitrate maintained high performance over time, whereas CZA_chloride deactivated due to coke formation, likely caused by $CuAl_2O_4$ phases limiting Cu/ZnO synergy. Comparison with a commercial $Cu/ZnO/Al_2O_3$ catalyst (CZA_commercial) revealed that while both catalysts were active, CZA_nitrate significantly outperformed the commercial catalyst, achieving higher methanol selectivity (100 % vs. 23 %) at WHSV of 10 h^{-1}, and 1 bar. At elevated pressures (up to 7 bar), methanol selectivity remained high at lower temperatures, while at 250 °C, increased pressure mitigated RWGS side reactions, enhancing selectivity. Methane formation remained negligible across all conditions, confirming that the primary side reaction was the RWGS reaction. A comparison with literature data demonstrated that CZA_nitrate outperformed previously reported Cu-based catalysts at atmospheric pressure, achieving superior methanol selectivity even at low temperatures (180–200 °C). This study highlights CZA_nitrate as an optimized catalyst for CO_2 hydrogenation and emphasizes the crucial role of precursor selection in designing highly efficient Cu-based catalysts for selective CO_2 conversion to methanol.

* Corresponding authors.
E-mail addresses: serena_esposito@polito.it (S. Esposito), giiervolino@unisa.it (G. Iervolino).

https://doi.org/10.1016/j.cej.2025.169870
Received 17 July 2025; Received in revised form 7 October 2025; Accepted 18 October 2025
Available online 22 October 2025

1. Introduction

The global demand for sustainable energy solutions has grown exponentially in response to rising concerns about climate change, primarily driven by anthropogenic greenhouse gas (GHG) emissions [1,2]. Carbon dioxide (CO_2), the most significant GHG, accounts for approximately 75 % of global emissions, originating mainly from the combustion of fossil fuels for energy production, industrial processes, and transportation activities [3–6]. To achieve the objectives set by the Paris Agreement—which aims to limit global warming to well below 2 °C compared to pre-industrial levels—it is essential to reduce CO_2 emissions and transition towards carbon-neutral energy systems. In this context, the development of renewable and low-carbon fuels, such as methanol produced via CO_2 hydrogenation, is becoming increasingly important [3,7]. Methanol, a versatile chemical feedstock and energy carrier, has gained significant attention as a potential green fuel [3,5]. Traditionally derived from fossil sources such as natural gas and coal [8], methanol production has been a notable contributor to GHG emissions. However, the recent shift towards utilizing CO_2 as a feedstock for methanol synthesis presents a promising strategy to close the carbon loop [3,9]. This process, commonly referred to as CO_2 hydrogenation, involves the catalytic conversion of CO_2 and green hydrogen (H_2)—generated from renewable energy sources such as wind, solar, or hydropower—into methanol. The advantage of this approach lies in its potential to produce methanol with a minimal carbon footprint, transforming CO_2 from a pollutant into a valuable resource [10,11]. The urgency to develop scalable and efficient CO_2 hydrogenation technologies arises from the numerous benefits they offer. First, methanol produced via this method can serve as a drop-in replacement for fossil-based methanol in the chemical industry, reducing dependence on non-renewable resources [12]. Second, as a liquid fuel, methanol can be directly utilized in internal combustion engines, fuel cells, or as a precursor for synthetic fuels, providing a viable alternative to conventional fuels in hard-to-decarbonize transportation sectors, such as shipping and aviation [13]. Lastly, large-scale implementation of CO_2 hydrogenation to methanol could significantly contribute to the decarbonization of the energy sector by integrating renewable hydrogen production with CO_2 capture and utilization (CCU) strategies [4,14,15].

The choice of catalyst is crucial for both process selectivity and efficiency. Recent research efforts have been dedicated to developing and optimizing catalytic systems to enhance conversion rates, methanol selectivity, and catalyst stability. Among the various catalysts studied, Cu-based catalysts remain the most widely explored for methanol production via CO_2 hydrogenation. In particular, Cu-ZnO/Al_2O_3 catalysts, traditionally used for methanol synthesis from syngas (CO and H_2), have been extensively investigated for CO_2 hydrogenation due to their high activity and commercial relevance [5,16–20]. Recent research has focused on enhancing the interaction between copper and the metal oxide support, which plays a crucial role in facilitating CO_2 adsorption and activation. For instance, modifications with Ga_2O_3 [21,22] and ZrO_2 [23] have been shown to improve methanol selectivity by promoting the formation of formate intermediates, which are essential for methanol synthesis from CO_2. Additionally, ZrO_2 doping enhances the dispersion of copper particles, leading to improved catalyst stability and performance. Boron oxide-modified CuO/ZnO catalysts exhibit enhanced activity and stability at lower temperatures due to a reduction in activation energy [24]. Similarly, La_2O_3-promoted CuO/ZnO/Al_2O_3 catalysts, despite showing a decrease in CO_2 conversion, achieve higher methanol selectivity and yield [25]. This study aims to investigate the influence of different copper and zinc precursor salts on the catalytic performance of Cu/ZnO/Al_2O_3 catalysts in CO_2 hydrogenation to methanol. While previous studies have explored synthesis strategies—such as direct or reverse co-impregnation [26], the use of different precursor salts to understand the changes in the synthesis steps or in the precipitation mechanism [27,28], to our knowledge, no existing research has systematically correlated the nature of Cu and Zn precursor salts with the formation of Cu/ZnO interfacial sites and their direct impact on catalytic performance in CO_2 hydrogenation to methanol. In this work, Cu/ZnO/Al_2O_3 catalysts were synthesized via a wet impregnation–co-impregnation method using nitrate, acetate, or chloride precursors for CuO and ZnO. A comprehensive characterization campaign—employing N_2 physisorption, Temperature-Programmed Reduction (TPR), X-ray Diffraction (XRD), Raman spectroscopy, UV–Vis DRS, High-Resolution and X-ray Photoelectron Spectroscopy (XPS), FESEM, STEM—was conducted to investigate textural, structural, redox, morphological, and surface chemical properties. Catalytic performance was evaluated over a wide range of temperatures (180–350 °C) and pressures (1–7 bar), with a focus on methanol selectivity and productivity. Stability tests were also carried out under the most favorable conditions.

2. Materials and methods

2.1. Reagents used for catalysts preparation

Copper(II) nitrate trihydrate (Sigma-Aldrich), zinc nitrate hexahydrate (Sigma-Aldrich), copper(II) chloride dihydrate (Sigma-Aldrich), zinc chloride anhydrous (Sigma-Aldrich), copper(II) acetate anhydrous (Sigma-Aldrich), and zinc acetate dihydrate (Sigma-Aldrich) were used as precursor salts. Al_2O_3 (Puralox), calcined at 600 °C, was employed as the support. Bi-distilled water was used for the preparation of the salt solution. Commercial catalyst was supplied by Thermo Fisher Scientific. According to the manufacturer's specifications, its composition is as follows: 63.8 wt% CuO, 24.6 wt% ZnO, 9.9 wt% Al_2O_3, and 1.4 wt% MgO.

2.2. Catalysts preparation

The Cu/ZnO/Al_2O_3 catalyst was synthesized using the wet co-impregnation method. Three different samples were prepared by employing nitrate, acetate, and chloride as Cu and Zn precursor salts.

The precursor salts were first dissolved in distilled water and stirred until completely dissolved. Al_2O_3 was then added to the solution, and the mixture was subjected to ultrasonic treatment to achieve a homogeneous dispersion. Subsequently, the solution was continuously stirred and dried at 80 °C. Once the solvent had completely evaporated, the resulting dry sample was calcined in static air at 600 °C for 1 h, using a heating ramp of 5 °C min^{-1}. At the end of the preparation process, catalysts with a nominal composition of 30 wt% CuO, 55 wt% ZnO, and 15 wt% Al_2O_3 were obtained, with particle sizes ranging from 180 to 355 μm. The catalysts were named CZA_nitrate, CZA_acetate, and CZA_chloride for the Cu/ZnO/Al_2O_3 samples prepared using nitrates, acetates, and chlorides as precursor salts, respectively.

2.3. Catalysts characterization

All prepared samples were characterized using various analytical techniques. Specific surface area (SSA) analysis was performed using the BET method with N_2 adsorption at −196 °C, employing a Costech Sorptometer 1042.

The Raman spectra were recorded using a Dispersive MicroRaman system (Invia, Renishaw), equipped with a 514 nm laser, in the 100–2000 cm^{-1} Raman shift range. Before conducting the catalytic activity tests, Temperature Programmed Reduction (TPR) analysis was performed using a 500 Ncm^3 min^{-1} flow of a hydrogen/argon mixture containing 5 vol% H_2, while the temperature was increased to 600 °C at a heating rate of 5 °C min^{-1}.

The UV-A–Vis diffuse reflectance spectra (UV-A–Vis DRS) of the catalysts were acquired using a Perkin Elmer Lambda 35 spectrophotometer, equipped with an RSA-PE-20 reflectance spectroscopy accessory (Labsphere Inc., North Sutton, NH).

X-ray powder diffraction (XRD) analysis was carried out using a Philips X'Pert diffractometer with Cu Kα radiation. The scanning was

performed in a 2θ range of 20°–90° with a step size of 0.02° 2θ and a time per step of 100 s. The lattice parameters of the fluorite phase present in the samples were determined through unit cell refinement using UnitCell software and the crystallite size was determined by applying the Scherrer formula. TPD analysis was performed on 0.1 g of the catalysts using a Micromeritics AutoChem II Instrument equipped with a thermal conductivity detector. For NH_3 -TPD, the samples were exposed to a 2 vol% NH_3 /He mixture (flow rate of 55 cm 3 /min) at room temperature for 30 min to allow complete adsorption of ammonia onto the acid sites; then, the samples underwent a 50 cm 3 /min He flow and a heating rate of 10 °C min^{-1} from room temperature to 550 °C. A similar procedure was used for CO_2-TPD, where the samples were first saturated at room temperature under a 15 vol% CO_2 /N_2 mixture (flow rate of 50 cm 3 /min), followed by a He purge and heating up to 550 °C under the same He flow. Signals were integrated as a function of time on stream; a preliminary calibration allowed us to determine the response factors for the conversion of NH_3 or CO_2 signals measured by the TC detector into amount (in mmol). Samples were not pre-treated. X-ray Photoelectron Spectroscopy (XPS) analysis was performed by means of a Physical Electronics PHI 5000 Versaprobe II spectrometer, with a monochromatic Al K-alpha line (1486.6 eV), with a dual compensation charge system made up of electron beam and Ar ions. Survey spectra have been acquired with a Pass Energy (PE) value of 187.85 eV, while High Resolution (HR) spectra have been acquired with PE = 23.50 eV. Time-per-step integration has been fixed equal to 20 ms for the survey and 50 ms for HR spectra, respectively. CasaXPS version 2.3.18 software has been employed to perform XPS spectra analysis. Background signals have been subtracted by means of the Tougaard function and C1s peak located at 284.8 eV has been chosen as reference for the Binding Energy axis. A commercial CuO powder has been used for Cu^{2+} reference in the Cu2p region analysis, while an Al foil, sputtered with Ar ions for 35 min at 2 kV accelerating voltage, has been used as reference for Al^0 and AlO_x in the Al2p region (residual O amount equals 1.5 at.%). Field-Emission Scanning Electron Microscopy (FESEM) was carried out with an Auriga FIB-SEM instrument (Zeiss) to study the morphology of the CZA catalysts.

Scanning Transmission Electron Microscopy (STEM) characterization was performed with a Thalos F200X instrument (ThermoFisher) equipped with four Silicon drift detectors (SDD) for Energy Dispersive X-ray spectroscopy (EDX). Concerning the sample preparation, the CZA_nitrate powder was dispersed in ultra-pure ethanol and subsequently drop-casted onto an Au lacey carbon grid. Before insertion in the TEM column, the sample was plasma-cleaned in an Ar atmosphere. Thermo Scientific Velox software was used for the analysis of images and EDX data. EDX maps were obtained by evaluating the integrated intensity of the peaks after subtraction of the background.

2.4. Catalytic activity tests

Catalytic activity tests were conducted in a tubular stainless steel reactor (Length: 350 mm, Diameter: 11 mm, Thickness: 1.5 mm) placed inside an electric oven controlled by a TLK 43 (Ascon Technologic). The catalyst (particle size 180–355 μm) was mixed with quartz (particle size 355–500 μm) and positioned inside the reactor between two layers of glass wool in the isothermal zone to ensure flow homogenization. The feed stream was introduced into the reactor using Mass Flow Controllers (Bronkhorst), maintaining a CO_2:H_2 ratio of 30:70 vol%. The outlet stream composition was analyzed using a mass spectrometer (Hiden HPR20), while the reactor temperature was monitored by two thermocouples placed at the inlet and outlet of the catalytic bed. To compare the three catalysts, methanol selectivity (S_{CH_3OH}), methanol TOF, and stability were assessed. Methanol selectivity was calculated using Eq. (1), methanol TOF via Eq. (2), and stability was evaluated at the optimal operating conditions. Catalytic performance was evaluated under different Weight Hourly Space Velocities (WHSV, Eq. 3) (10, 20, 25, and 30 h^{-1}) while varying the reaction temperature from 180 °C to 350 °C. All screening tests were performed at atmospheric pressure. The catalyst that exhibited the best performance was compared with the commercial catalyst (CZA_commercial) (Thermo Fisher) and further tested in the pressure range of 1–7 bar.

The mathematical relationships used to evaluate S_{CH_3OH}, TOF (Turnover Frequency), and WHSV are provided below:

$$S_{CH_3OH}[\%] = \frac{P_{CH_3OH}}{P_{CH_3OH} + P_{CH_4} + P_{CO}} \cdot 100 \quad (1)$$

$$TOF\left[h^{-1}\right] = \frac{P_{CH3OH}\left[\frac{mol}{h}\right]}{Cu[mol]} \quad (2)$$

$$\mathrm{WHSV} = \frac{W_{IN}\left[\frac{g}{h}\right]}{g_{catalyst}} \quad (3)$$

$$P_{CH_3OH}\left[\mu\frac{mol}{min}\right] = \frac{Y_{CH3OH} * F_{IN}}{22414} \quad (4)$$

where: P_{CH3OH} is the methanol productivity, P_{CH4} methane productivity, and P_{CO} carbon monoxide productivity; W_{IN} is the inlet flow in g h^{-1}, Y_{CH3OH} is the molar fraction of methanol in the outlet gas stream, and F_{IN} is the inlet volumetric flow.

2.5. Post-reaction temperature programmed oxidation (TPO)

TPO (Temperature Programmed Oxidation) analysis was performed after the catalytic activity tests to evaluate coke formation during the reaction. The test was conducted at atmospheric pressure using a feed gas mixture of Ar and O_2 at a 95:5 vol% Ar:O_2 ratio, with a total flow rate of 500 Ncm^3 min^{-1} and a heating ramp of 5 °C min^{-1}. During the test, the formation of CO and CO_2 was continuously monitored using a mass spectrometer (Hiden HPR20).

3. Results and discussion

3.1. Catalyst characterization

The influence of varying copper and zinc precursors on the crystallinity of CZA samples was studied using X-ray diffraction (XRD). The resulting XRD patterns are shown in Fig. 1a. Detailed phase analysis identified diffraction peaks associated with alpha-alumina (JCPDS card n° 10–0173 square symbol, □), wurtzite zinc oxide (JCPDS card n° 36–1451 rhombus symbol, ◊), and copper (JCPDS card n° 48–1548 asterisk symbol, *).

The CZA_chloride sample exhibits more pronounced CuO peaks (notably at 35.54, 38.71, 48.71, and 53.49, where 35.54 and 38.71 correspond to 100 % and 90 % intensity, respectively), which implies a diminished dispersion of the copper oxide. Indeed, using Scherrer's formula, the average CuO crystallite size was determined to be about 20 nm for samples prepared from nitrates and acetates, and roughly 35 nm for CZA_chlorides. Additionally, the CZA_nitrate sample shows significantly higher relative intensities of zinc oxide peaks compared to what is observed in the CZA_chloride and CZA_acetate patterns. Magnification of the diffraction patterns in the 2-theta range of 30°-60°, Fig. 1b, reveals another significant difference: the presence of signals that can be attributed to the formation of a copper aluminate phase, $CuAl_2O_4$ (JCPDS card n° 33–0448), supporting the reduction behavior revealed by H_2-TPR analysis (vide infra).

An analysis of the Specific Surface Area (SSA) was conducted for all the prepared samples, as well as for the Al_2O_3 support used in catalyst preparation (annealed at 600 °C). This analysis aimed to evaluate how the impregnation of Cu and Zn species influences the surface area of the final catalyst.

The BET method was employed to determine SSA values, and the

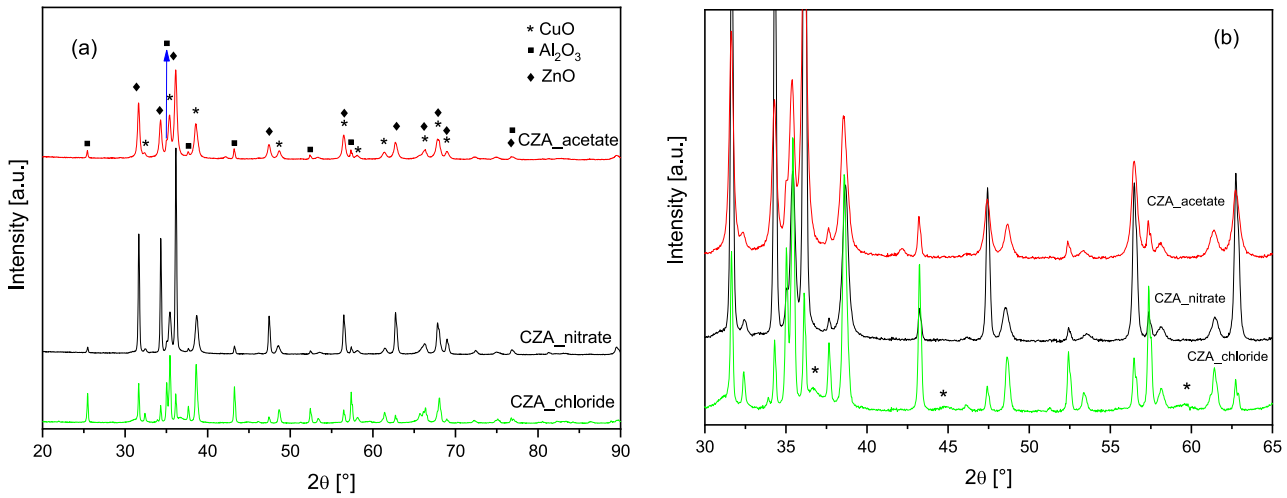

Fig. 1. (a) XRD patterns of the catalysts CZA_nitrate, CZA_acetate, and CZA_chloride; (b) enlargement of the XRD patterns in the 2-theta range 30°-65°.

results are presented in Table 1.

As observed, all synthesized catalysts exhibited a notable reduction in surface area compared to pure Al_2O_3 (18 m^2/g), which serves as the support material. This decrease is expected, as the introduction of CuO and ZnO phases can lead to partial support pore blocking or increased particle agglomeration [29]. Among the prepared catalysts, CZA_nitrate showed the most significant decrease in SSA (3 m^2/g), while CZA_acetate retained a higher surface area (11 m^2/g), followed by CZA_chloride (9 m^2/g). The differences in SSA among the samples suggest that the choice of precursor salts influences the dispersion and deposition of CuO and ZnO onto the Al_2O_3 surface. In particular, nitrate precursors appear to induce a stronger reduction in SSA, possibly due to differences in precursor decomposition behavior during calcination, which may promote a higher degree of pore blockage [27]. This trend aligns with previous findings that precursor chemistry plays a crucial role in determining textural properties of Cu/ZnO-based catalysts. Phongprueksathat et al. [27] reported that catalysts prepared from nitrate precursors exhibit a stronger interaction with the support, often leading to lower SSA but enhanced metal-support interactions. Conversely, acetate precursors may favor a more homogeneous metal dispersion, helping to preserve a greater fraction of the original porosity [27]. Similarly, Lee et al. [29] demonstrated that the selection of the metal precursor significantly impacts the catalyst specific surface area. So, although CZA_nitrate exhibited the lowest BET surface area (3 m^2/g), this does not translate into poorer catalytic performance. On the contrary, the nitrate precursors promote strong metal–support interactions and intimate Cu–ZnO–Al_2O_3 domains, which reduce the global SSA but increase the density of active Cu–ZnO interfaces. This finding highlights that total surface area is not a reliable descriptor of catalytic activity in these systems; rather, the nanoscale distribution and connectivity of the phases govern methanol selectivity and productivity.

The Raman spectra of the synthesized catalysts, along with commercial CuO and ZnO, are shown in Fig. 2.

The comparison with pure CuO and ZnO reveals notable spectral shifts and modifications, providing insights into metal-support interactions, CuO dispersion, and the formation of the CuO/ZnO interface,

Table 1
Specific Surface Area (BET) analysis results.

Sample	SSA [m^2/g]
Al_2O_3	18
CZA_nitrate	3
CZA_acetate	11
CZA_chloride	9

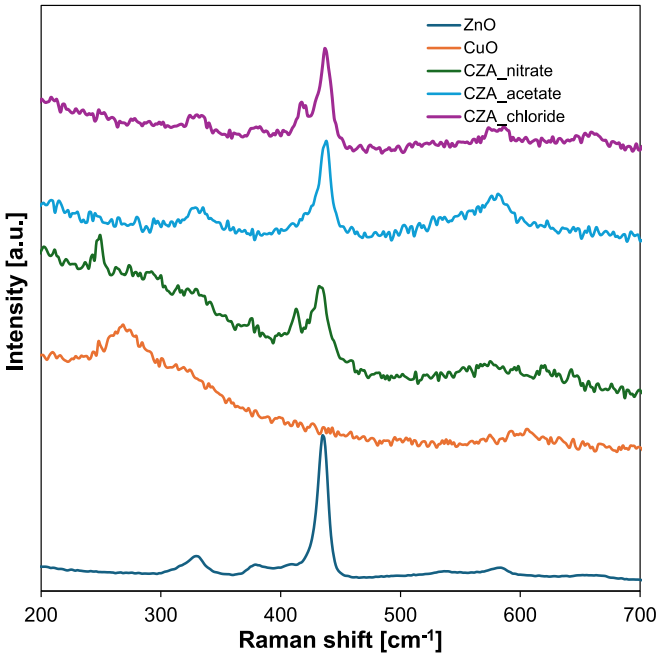

Fig. 2. Raman spectra of ZnO, CuO, CZA_nitrate, CZA_acetate, and CZA_chloride.

which plays a key role in CO_2 hydrogenation performance [30,31]. The CuO reference spectrum exhibits characteristic vibrational modes at about 266 cm^{-1} and 328 cm^{-1} associated with A_g and $B_g^{(1)}$ phonon modes along with a broader Raman band in the range 570–625 cm^{-1} ($Bg^{(2)}$) associated with monoclinic CuO [30,32–34]. The ZnO reference spectrum, on the other hand, shows a strong peak at 434 cm^{-1}, attributed to the E_2(high) mode of ZnO, characteristic of the wurtzite structure [35]. The spectral features observed in the synthesized catalysts generally match these references, but shifts and intensity variations indicate significant structural modifications. A key observation is that the 266 cm^{-1} CuO peak is absent or highly suppressed in CZA_acetate and CZA_chloride, while it is downshifted in CZA_nitrate. This behavior suggests a strong precursor-dependent effect on the structural properties of the CuO phase. In CZA_nitrate, the 266 cm^{-1} peak appears narrowed and downshifted, which may be attributed to the quantum confinement effect of the CuO nanoparticles [34]. In contrast, the absence of the 266 cm^{-1} peak in CZA_acetate and CZA_chloride suggests that CuO in these

samples is either highly dispersed or structurally modified to the extent that the typical CuO vibrational mode is no longer detectable. This could be due to Cu^{2+} incorporation into the ZnO lattice during the thermal annealing process, leading to a loss of the distinct CuO vibrational signature [36,37]. The 434 cm^{-1} ZnO peak remains well-defined in all samples, indicating that the ZnO lattice structure is largely preserved across the catalysts. However, notable differences in peak broadening and intensity variations suggest modifications in CuO/ZnO interactions. For CZA_nitrate, the 434 cm^{-1} peak exhibits slight broadening compared to pure ZnO, which suggests an increased CuO/ZnO interfacial interaction without severe strain effects [36]. This behavior is consistent with a well-integrated CuO/ZnO system, where CuO is finely dispersed but does not induce significant distortions in the ZnO lattice. In contrast, for CZA_acetate and CZA_chloride, the 434 cm^{-1} peak appears more pronounced and slightly narrower, suggesting that CuO particles in these samples may be less dispersed or interacting differently with ZnO. A well-defined E_2(high) mode with reduced broadening generally indicates a lower degree of lattice strain and fewer defect-related modifications in ZnO, implying that in these two samples, CuO exists more as separate particles rather than forming an extensive CuO/ZnO interface. This interpretation aligns with previous studies that reported broader ZnO peaks in catalysts where metal oxides were better dispersed and more interactive with the support, whereas sharper peaks indicated more phase-segregated systems [38]. Additionally, for CZA_nitrate, the A_1(LO) mode at 574 cm^{-1} of ZnO [39] is relatively weak, suggesting fewer defect-related vibrations and a more ordered ZnO lattice. However, a strong band at ~418 cm^{-1} (assigned to E_1(TO) mode of ZnO) is observed, which is not present in either CuO or ZnO but has been attributed to the presence of oxygen vacancies [40], indicating the presence of Cu-O-Zn interactions at the Cu-ZnO interface. The CZA_acetate spectrum shares similarities with CZA_nitrate but exhibits broader CuO-related bands and a weaker 418 cm^{-1} feature, indicating that CuO/ZnO interactions are less pronounced. The A_1(LO) mode at 574 cm^{-1} is more intense than in CZA_nitrate, suggesting a higher density of oxygen vacancies. The CZA_chloride spectrum differs significantly, particularly in the 600–700 cm^{-1} range, where a broad band is observed. This feature is indicative of $CuAl_2O_4$ (copper aluminate spinel), a phase that forms when Cu strongly interacts with Al_2O_3 rather than ZnO [41]. This finding aligns with XRD (Fig. 1) and TPR results (vide infra), further confirming that a significant fraction of Cu is trapped in the $CuAl_2O_4$ phase.

The UV–Vis DRS spectra of the synthesized catalysts are shown in Fig. 3.

Compared to pure ZnO, which exhibits a sharp absorption edge at ~370 nm, the CZA_nitrate and CZA_acetate samples display an extended visible-light absorption up to ~800 nm, suggesting a significant modification of their electronic structure due to the incorporation of CuO species. This extended absorption is consistent with the formation of a CuO/ZnO interface [42]. The CZA_nitrate spectrum exhibits two distinct absorption features, a broad band at 600–700 nm and a second band at 760–770 nm. The first has been attributed to finely dispersed CuO phases, while the second is associated with d-d transitions of isolated Cu^{2+} ions in a tetragonally distorted octahedral environment [43]. A similar absorption band at 600–700 nm is observed in CZA_acetate, reinforcing the hypothesis that both catalysts contain well-dispersed CuO species.

A distinct absorption pattern is observed for CZA_chloride, where the spectrum features a broader absorption in the visible region with three peaks: one at 680 nm, corresponding to finely dispersed CuO species, and two additional bands at 720 nm and 770 nm. The peaks beyond 700 nm indicate the presence of bulk CuO [44], but also suggest the formation of $CuAl_2O_4$, a copper-aluminate spinel phase, which has been reported to exhibit a characteristic d-d transition in the 700–800 nm region, associated with Cu^{2+} ions in an octahedral coordination within the spinel structure [45]. The presence of $CuAl_2O_4$ in this sample was further supported by XRD results (Fig. 1), Raman (Fig. 2) and TPR analysis (vide infra).

The H_2-TPR profiles of the CZA_nitrate, CZA_acetate, and CZA_chloride catalysts (Fig. 4) reveal distinct reduction behaviors, highlighting differences in CuO dispersion, Cu-ZnO interactions, and the presence of additional phases.

The first reduction peak, observed between 170 and 250 °C, is well-defined for CZA_nitrate and CZA_acetate, while it is weakly present in CZA_chloride. This peak corresponds to the reduction of finely dispersed CuO species and CuO interacting at the Cu/ZnO interface [46,47]. The CZA_nitrate catalyst exhibits a more intense reduction peak compared to CZA_acetate, indicating a higher fraction of reducible CuO species. In contrast, CZA_acetate exhibits a broader and less intense first reduction peak, indicating a significantly lower fraction of reducible CuO, suggesting that CuO is not well-dispersed. Moreover, the second reduction peak, located in the 350–470 °C range, is most prominent in CZA_chloride, confirming the presence of strong Cu—Al interactions leading to $CuAl_2O_4$ formation [48]. $CuAl_2O_4$ is a stable spinel phase, in which Cu^{2+} is trapped in octahedral coordination with Al [43], making it much less reducible than dispersed CuO. The broad nature of this peak confirms that Cu-species reduction in CZA_chloride is difficult. For CZA_nitrate and CZA_acetate, the second peak is almost absent, confirming that Cu is primarily present in a reducible, dispersed form rather than in a strongly bound $CuAl_2O_4$ phase. The absence of this high-temperature reduction feature in these two samples is consistent with their higher catalytic performance (vide infra).

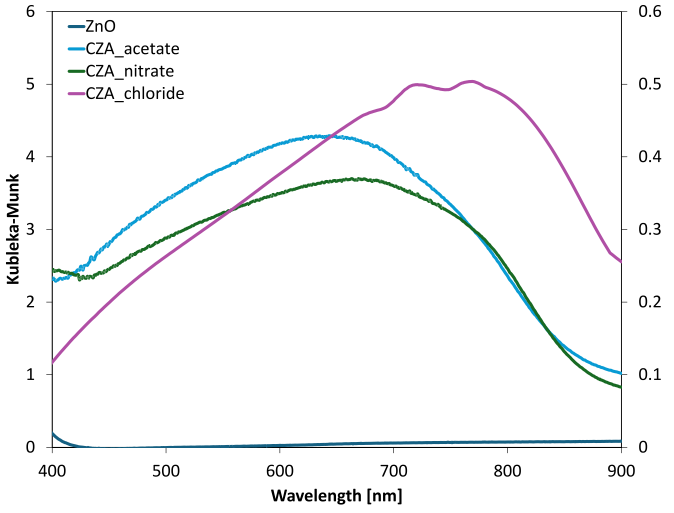

Fig. 3. UV–Vis DRS spectra of CZA_nitrate, CZA_acetate, CZA_chloride, and ZnO.

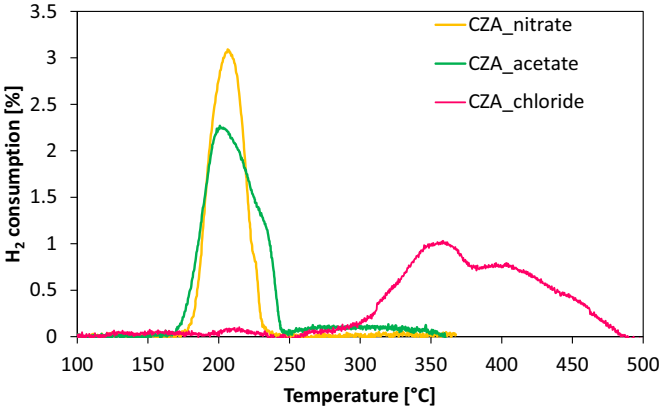

Fig. 4. H_2-TPR profiles of CZA_nitrate, CZA_acetate, and CZA_chloride catalysts.

A more detailed deconvolution analysis of the first reduction peak in the H_2-TPR profiles (Fig. 5), combined with a quantitative assessment (Table 2), reveals critical differences in Cu/ZnO interactions and metal dispersion among the CZA_nitrate, CZA_acetate, and CZA_chloride catalysts [49].

The first reduction peak (A) is attributed to finely dispersed CuO, which is highly reducible due to its small particle size and weak interaction with the support [46]. The second reduction peak (B) corresponds to CuO species interacting at the Cu/ZnO interface, forming a partially reducible phase [47,50]. The third reduction peak (C) is associated with small CuO clusters [50–52].

The peak A is dominant in CZA_acetate (63.6 %) and significantly lower in CZA_nitrate (38.7 %), while it is absent in CZA_chloride (Table 2), indicating a lack of highly dispersed CuO species in this latter sample. The higher intensity of peak A in CZA_acetate suggests a greater fraction of isolated CuO nanoparticles, which are more easily reducible. On the other hand, the CZA_nitrate catalyst exhibits the highest fraction of peak B (60.3 %), confirming the presence of a well-developed Cu/ZnO interface. In CZA_acetate, this peak represents only 28.2 %, suggesting that although CuO is present, a smaller fraction is interacting with ZnO. CZA_chloride's peak B, is about 60.1 %, even though it seems comparable with the CZA_nitrate, the Cu moles at the interface is lower as it could be noticed in the Table 2 (TPR analysis show that CZA_chloride sample has a broader peak at high temperature, due to the $CuAl_2O_4$ while a smaller peak is reported at 210 °C, of that peak 60.1 % is Cu-ZnO interface), aligning with the previously discussed Raman and UV–Vis DRS analyses, which revealed limited CuO/ZnO interface formation in this sample. Furthermore, CZA_acetate exhibits the highest relative fraction of peak C (8.2 %), while in CZA_nitrate, this peak is minimal (1.0 %), confirming that CuO in CZA_nitrate is better dispersed and more effectively interacts with ZnO. In contrast, CZA_chloride presents a peak C fraction of 39.9 %, reinforcing the conclusion that this sample consists mainly of larger CuO aggregates. A key metric derived from these data is the $Cu_{interface}$ content, which quantifies the moles of CuO interacting with ZnO (Table 2). CZA_nitrate exhibits the highest $Cu_{interface}$ value (0.002 mol), followed by CZA_acetate (0.0011 mol), while CZA_chloride has an extremely low $Cu_{interface}$ content ($4.756*10^{-5}$ mol). These findings further reinforce that CZA_nitrate possesses the most favorable Cu/ZnO interface for catalytic applications. The higher Cu–ZnO interfacial density in CZA_nitrate correlates with stronger Cu–ZnO interactions, leading to superior performance in methanol synthesis (vide infra). Finally, Table 3 compares the theoretical CuO content with the experimental values calculated from the TPR profiles in Fig. 4 for the CZA_nitrate, CZA_acetate, and CZA_chloride catalysts. The results show that the experimental CuO content closely matches the nominal value of 30 wt%, confirming the accuracy of the synthesis procedure. Minor deviations between the theoretical and measured values may be attributed to experimental errors associated with H_2 consumption measurement during TPR or to Cu losses during the catalyst preparation process.

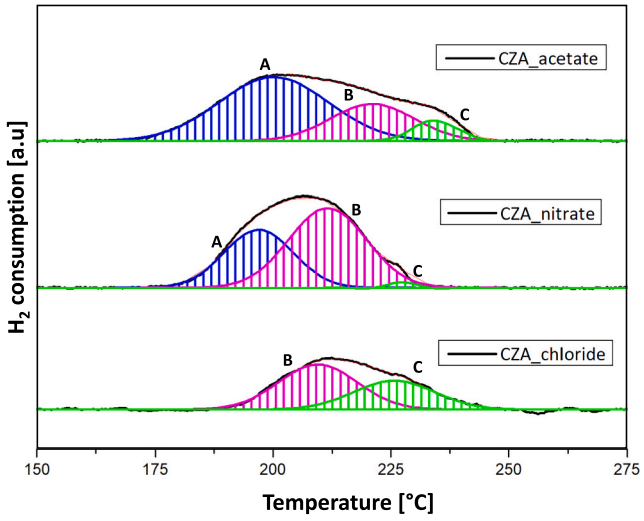

Fig. 5. Deconvolution of the first reduction peak in the H_2-TPR profiles of CZA_nitrate, CZA_acetate, and CZA_chloride catalysts. The reduction peaks are labeled as A, B, and C, corresponding to different CuO species.

Fig. 6a shows the NH_3-TPD profiles of CZA samples, while desorbed amounts are reported in Table 4 and in Fig. 6b. Three types of acid sites are generally identified as weak, moderate, and strong. There is no general consensus on the corresponding desorption temperatures [53–55]. CZA_acetate is characterized by a larger amount of acid sites (mostly moderate acid sites, with some low acidity as well), with the main desorption peak at 325 °C. CZA_chloride shows a low NH_3 desorption corresponding to moderate-low acidity, while CZA_nitrate is characterized by a low acidity with a wide desorption profile. The most evident difference among the samples is the large amount of NH_3 desorbed from CZA_acetate at medium temperature. Its attribution is not trivial. According to Li et al. [56], this peak could be attributed to CZA catalysts, while Catizzone et al. [57] reported desorption of NH_3 from γ-Al_2O_3 at 160 and 330 °C with a relative ratio equal to 1:3. Our results seem to support the attribution to alumina. In the other samples, the suppression of the intrinsic acidity of alumina could be due to the interaction among the different elements and/or to surface modifications due to the different precursors.

Fig. 7 shows the CO_2-TPD profiles normalized by catalyst mass of the investigated CZA samples, while desorbed amounts are reported in Table 4. Similarly to acid sites, basic sites are often classified as weak, moderate to strong [58,59]. CZA_acetate is characterized by a larger amount of basic sites and it displays a sharp and intense peak at 162 °C, which is typically associated with weak basic sites, and a smaller shoulder at 256 °C, suggesting the presence of moderate to strong basic sites. CZA_chloride and CZA_nitrate, on the other hand, show similar behaviors with a broad peak with a long tail up to 400 °C, which was deconvoluted to three Gaussian peaks attributed to weak (144–138 °C, respectively) and medium to strong (328–330 °C, respectively) basic sites. The weak basic sites (low desorption temperature) were assigned to the structural OH groups on surface catalysts, while moderate to strong basic sites were related to metal-oxygen pairs and the coordinately unsaturated O^{2-} ions [49]. Table 4 shows the ratio of basic to acidic sites. Interestingly, this ratio increases with increasing catalytic performance, suggesting that this parameter influences the activity more than the overall amount of basic and/or acidic sites. Moreover, as shown in the CO_2-TPD profiles, the CZA_nitrate sample exhibits a greater capacity for CO_2 adsorption at higher temperatures (higher than 300 °C), which can be attributed not only to the highest basic-to-acid site ratio among the three samples, but also to the combination of a lower number of acid sites – also weaker in strength – and a higher amount of stronger basic sites. CO_2-TPD and NH_3-TPD deconvolution peak are reported in Fig. S1 and Fig. S2.

X-ray Photoelectron Spectroscopy (XPS) was employed to determine the oxidation states of the various chemical species present on the surface of the three synthesized samples, each prepared using different precursors. From the survey spectra (see Fig. 8-a), the presence of Zn, Cu, O, and C is clearly evident. Detecting aluminum (Al), originating from the alumina matrix, is more challenging, as the Al2p and Al2s regions are largely overlapped by the Cu3p and Cu3s peaks. Therefore, the reported relative atomic concentrations include only the aforementioned elements, excluding Al.

As shown in Table 5, the sample with the highest copper content is CZA_nitrate, while CZA_acetate has the lowest, with CZA_chloride displaying a similar intensity to the latter. Regarding zinc, the highest amount is found in the CZA_acetate sample, whereas the lowest is in CZA_chloride. Notably, the CZA_chloride sample exhibits a significantly higher oxygen content—over 10 atomic percent more than the other two samples. Given the low levels of both Cu and Zn in this sample, the

Table 2
Peak area, relative content, and Cu-ZnO interfacial Cu content ($Cu_{interface}$).

Catalyst	Peak area			Relative content (A_{Peak}/A_{Total})(%)			$Cu_{interface}$ [b] (mol)
	A_A	A_B	A_C	A_A/A_{Total} [a] (%)	A_B/A_{Total} [a] (%)	A_C/A_{Total} [a] (%)	
CZA_nitrate	35.70	55.10	0.81	38.7	60.3	1.0	0.002
CZA_acetate	62.47	27.70	8.13	63.6	28.2	8.2	0.00107574
CZA_chloride	/	1.19	0.79	/	60.1	39.9	$4.756*10^{-5}$

[a] A_A, A_B, and A_C are the areas of peaks A, B, and C, respectively, and A_{Total} is the sum of all peaks for each catalyst.
[b] Obtained from the deconvolution of the first reduction peak in the H_2-TPR profiles for CZA_nitrate, CZA_acetate, and CZA_chloride catalysts.

Table 3
Comparison between the theoretical CuO content (wt%) and the experimental CuO content (wt%) obtained from H_2-TPR analysis (Fig. 4) for CZA_nitrate, CZA_acetate, and CZA_chloride catalysts.

Sample	CuO theoretical [wt%]	CuO experimental [wt%]
CZA_nitrate	30	26.5
CZA_acetate	30	30.9
CZA_chloride	30	32.9

Table 4
Amount of NH_3 and CO_2 desorbed during NH_3/CO_2-TPD analysis for CZA_nitrate, CZA_acetate, and CZA_chloride.

Sample	NH_3 desorbed, mmol/g	CO_2 desorbed, mmol/g	CO_2/NH_3
CZA_acetate	1.8	0.9	0.5
CZA_chloride	0.9	0.7	0.7
CZA_nitrate	0.7	0.6	0.8

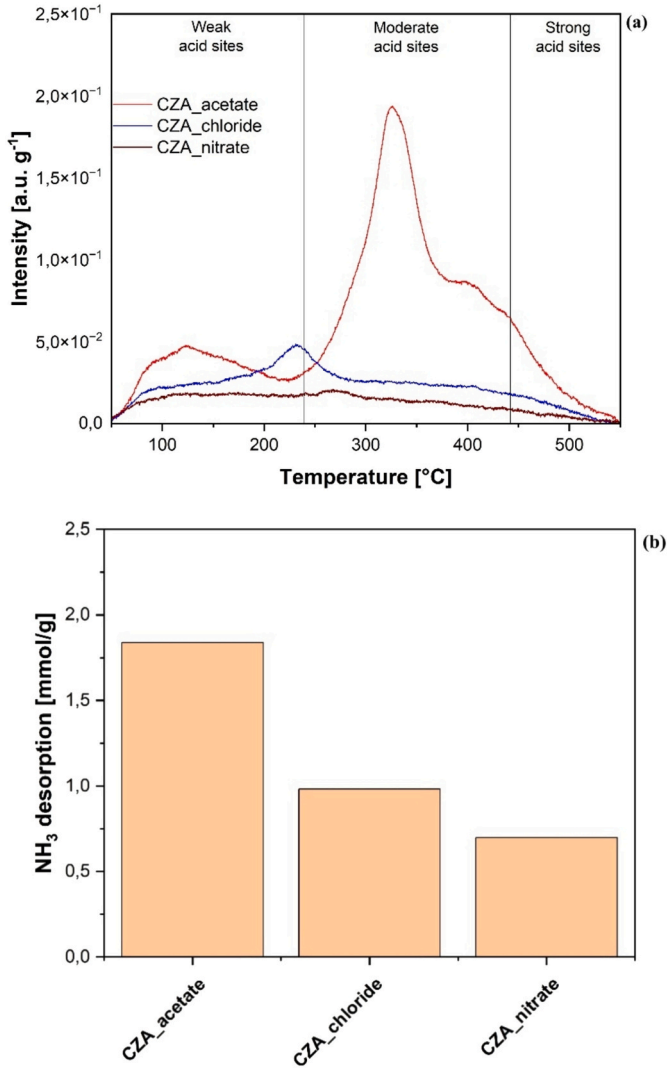

Fig. 6. NH_3-TPD profiles (a) and desorbed amounts (b) of CZA_nitrate, CZA_acetate, and CZA_chloride.

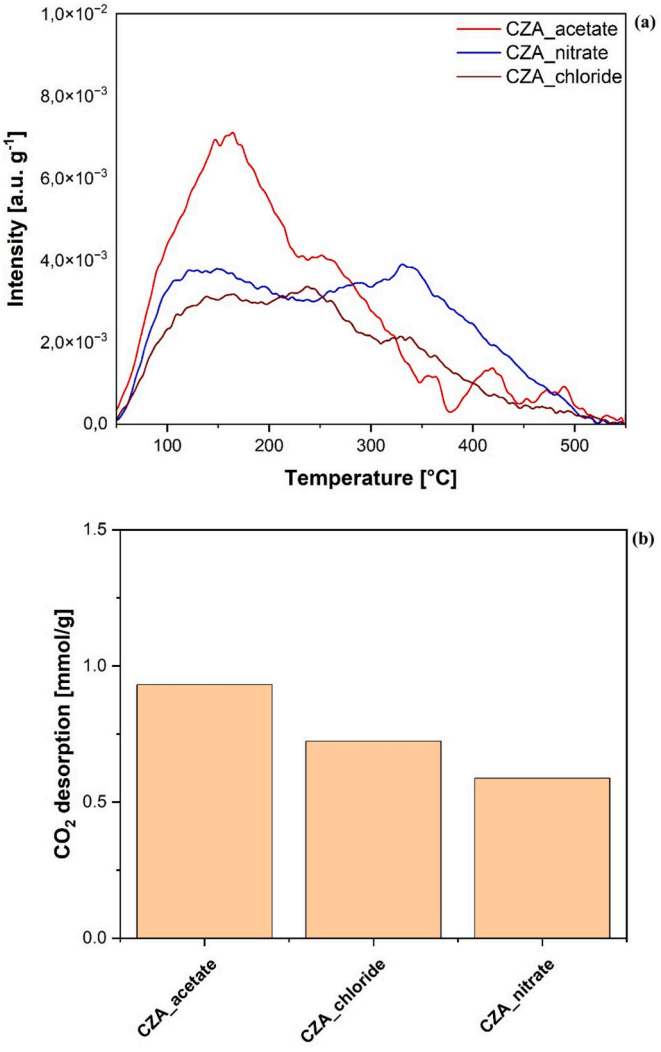

Fig. 7. CO_2-TPD profiles (a) and desorbed amounts (b) for CZA_nitrate, CZA_acetate, and CZA_chloride.

excess oxygen must be attributed to other chemical compounds. The detected carbon, likely from environmental contamination, is not sufficient to account for this increase in surface oxygen. Examining the

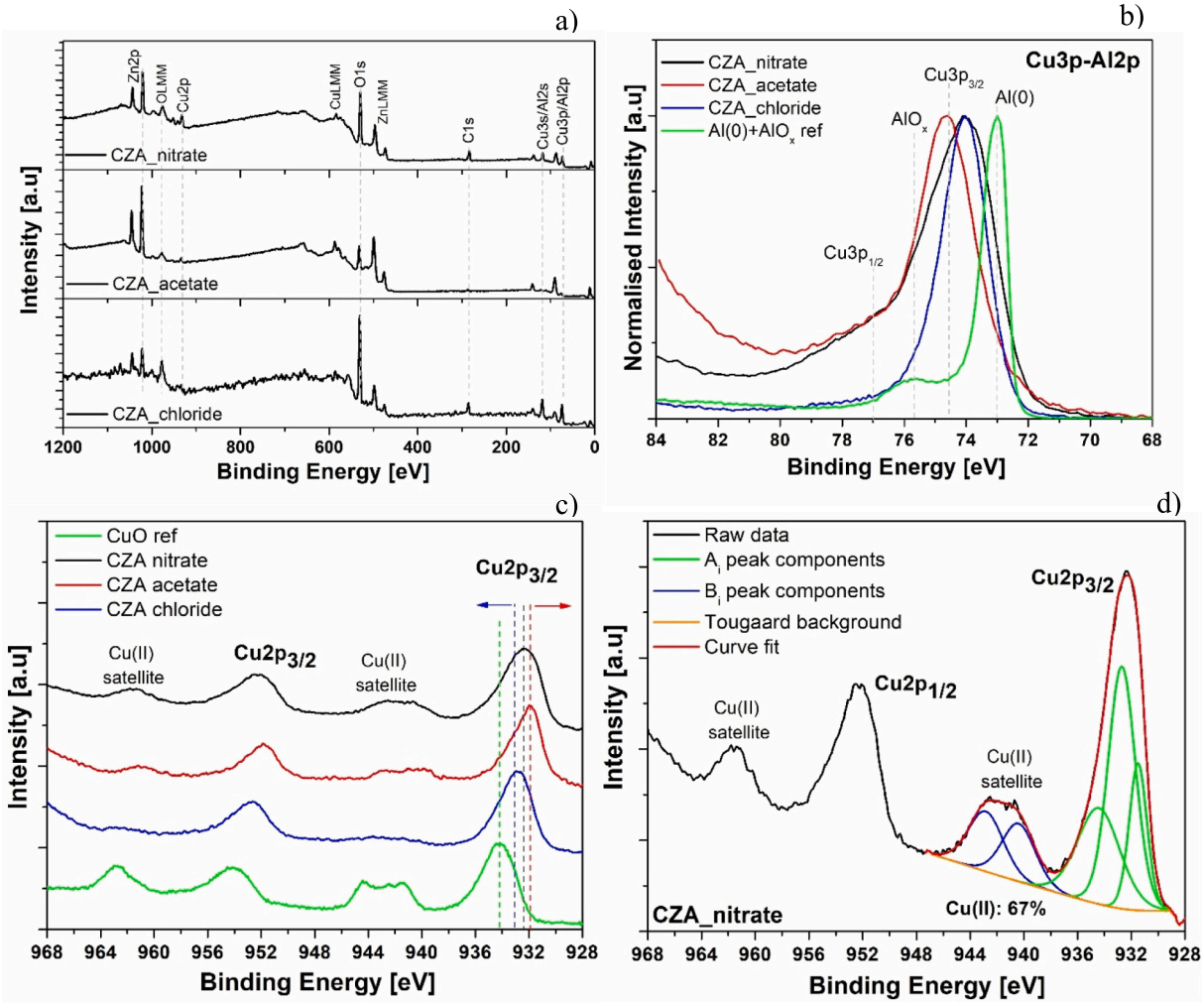

Fig. 8. XPS a) survey spectra for the three samples; b) Cu3p/Al2p high-resolution spectra to infer the presence of Al from the overlapping Cu. A reference spectrum has been added (green line) to highlight the position of Al metal and oxide; c) Cu2p doublets for the three samples and a CuO reference, showing the relative position of $Cu2p_{3/2}$ main peak and related Cu^{2+} satellite; d) the deconvolution peaks of the Cu2p region for CZA_nitrate sample, according to Biesinger et al. [61] method to evaluate Cu^{2+} concentration.

Table 5
XPS relative atomic concentration (at.%) for the three samples together with the calculation of the Cu^{2+}amount from Cu2p regions[a].

Sample	Relative atomic concentration [at.%]				Cu oxidation [%]
	C1s	O1s	$Cu2p_{3/2}$	$Zn2p_{3/2}$	Cu^{2+}
CZA_nitrate	30.5	57.1	3.7	8.7	67
CZA_acetate	14.6	58.1	2.1	25.2	44
CZA_chloride	19.1	72.2	2.6	6.1	30

[a] According to Biesinger et al. [61].

high-resolution (HR) spectra of the Cu3p/Al2p region (see Fig. 8-b), and comparing them with the spectrum of an aluminum metal foil with a thin oxide layer, we observe that the CZA_chloride spectrum is less asymmetric than those of the nitrate and acetate samples. It is also shifted towards lower binding energy (BE) values, which correspond to the expected position of AlOx peaks [60]. This observation aligns with previous characterizations that indicated the presence of $CuAl_2O_4$.

To further investigate the copper oxidation states, attention must be paid to the Cu2p HR region (Fig. 8-c). Copper is known to exhibit a significant chemical shift in the presence of Cu^{2+}, largely due to its electronic configuration, while Cu^0 and Cu^{1+} are mostly difficult to be distinguished in the Cu2p region, in the lower BE region [62]. Moreover, Cu^{2+} exhibits a well-known satellite in the 935–950 eV region, which makes easier the recognition of this species.

Starting from the CuO reference spectrum, we can see that the $Cu2p_{3/2}$ peak is located at a binding energy of around 934 eV and has a well-defined satellite, as expected. The CZA_nitrate sample is the one with the most intense satellite, although the position of the photoelectronic peak is shifted towards lower BE values (932.3 eV). The CZA_Acetate sample also has a very visible satellite, with the photoelectronic peak further shifted towards the decreasing BE scale (932.0 eV); we will come back to this point later. The CZA_chloride sample, on the other hand, is the one with the least intense satellite, but has the $Cu2p_{3/2}$ peak shifted towards higher BE values (932.9 eV), contrary to what one would expect, given the reduction in Cu^{2+} content. Examining the literature, we find an interesting work by I. S. Zhidkov et al. [63] where it is demonstrated how the peak in question shifts significantly to the left, in the presence of $CuAl_2O_4$ matrix, which further confirms the previous findings related to the presence of this compound.

If we want to obtain more objective data on the presence and abundance of Cu^{2+}, we can use the method presented by Biesinger et al. [61], which explains how, by using the ratio between the areas under the Cu $2p_{3/2}$ peak and its satellite (Fig. 8-d), and considering certain shape parameters of the satellite, it is possible to quantify the percentage of Cu^{2+} present. The remaining portion is attributed to Cu^0 and Cu^+, which cannot be distinguished in this region of the spectrum. To gain

more detailed information on Cu^0 and Cu^+, we would need to examine the Cu LMM Auger region. Unfortunately, in our case, this overlaps with the Zn LMM region, which limits the reliability of any deconvolution in that area. By looking at Table 5 (last column), we can clearly see that there is a linear trend starting from sample CZA_nitrate, with 67 % of Cu^{2+}, passing to CZA_acetate with 44 % and lastly CZA_chloride with 30 %. This trend follows the catalytic activity of the three samples, where CZA_nitrate is the most active and CZA_chloride the least active.

Since our hypothesis regarding catalytic activity is also based on enhanced surface interaction between ZnO and CuO, we analyzed the Zn $2p_{3/2}$ region as well. However, literature reports indicate that the assignment of the ZnO-related peak position is not unambiguous. This variability is often attributed to factors such as nanoparticle size, surface termination—which can lead to the formation of $Zn(OH)_2$ on the ZnO surface—and the material's porosity or compactness [64]. From the analysis of the three samples (not shown), we observe that the Zn $2p_{3/2}$ peak appears at a lower binding energy (1021.1 eV) for the CZA_acetate sample, with a full width at half maximum (FWHM) of 1.8 eV. For the CZA_nitrate sample, the peak shifts slightly to higher binding energy (1021.5 eV), with a FWHM of 2.7 eV. The CZA_chloride sample shows the largest shift to higher binding energy (1021.8 eV), with a FWHM of 2.4 eV. An increase in FWHM is typically attributed either to the presence of multiple oxidation states or to a certain degree of structural disorder, which creates inelastic interaction sites that alter the kinetic energy of the emitted photoelectrons. A different distribution of surface charge can also lead to broadening of the FWHM, as observed in the nitrate-based sample. G. Deroubaix and P. Marcus demonstrated in their work [65] that direct interaction between Cu and Zn shifts both the Zn $2p_{3/2}$ and Cu $2p_{3/2}$ peaks towards lower binding energy (BE) values. Specifically, in the presence of a Cu—Zn bond, the Zn $2p_{3/2}$ peak appears at 1021.5 eV and the Cu $2p_{3/2}$ peak at 932.7 eV, whereas in pure ZnO and CuO these peaks are located at 1022.1 eV and 933.6 eV, respectively. The CZA_nitrate and CZA_acetate samples show BE values more consistent with the Cu—Zn reference than with those of the individual oxides, suggesting possible charge transfer between the two components. In contrast, the CZA_chloride sample exhibits values closer to those of the unmodified oxides, indicating weaker surface interaction between Cu and Zn in this case.

FESEM images show that the morphology of the CZA catalysts is highly influenced by the choice of precursors. It is interesting to notice that the morphology at the nanoscale qualitatively correlates with the SSA values (Fig. S3).

Fig. 9 provides a representative STEM image of the CZA_nitrate catalyst, showing the complex, nanostructured morphology of its different components. It is interesting to correlate the morphology with the chemical composition by EDX mapping. Regions mostly dominated by the presence of the Al_2O_3 support are identified (right side of the STEM image in Fig. 9). Moreover, it is worth noticing that the EDX maps clearly prove that there are regions where Zn and Cu nanostructures are connected and homogeneously dispersed at the nanometer scale (left side of the STEM image in Fig. 9).

3.2. Catalytic activity results

3.2.1. Atmospheric pressure catalytic results

To assess the efficiency of the three prepared catalysts, activity tests were conducted under various operating conditions (varying WHSV and temperature). The tested WHSV values were 10, 20, 25, and 30 h^{-1}, and

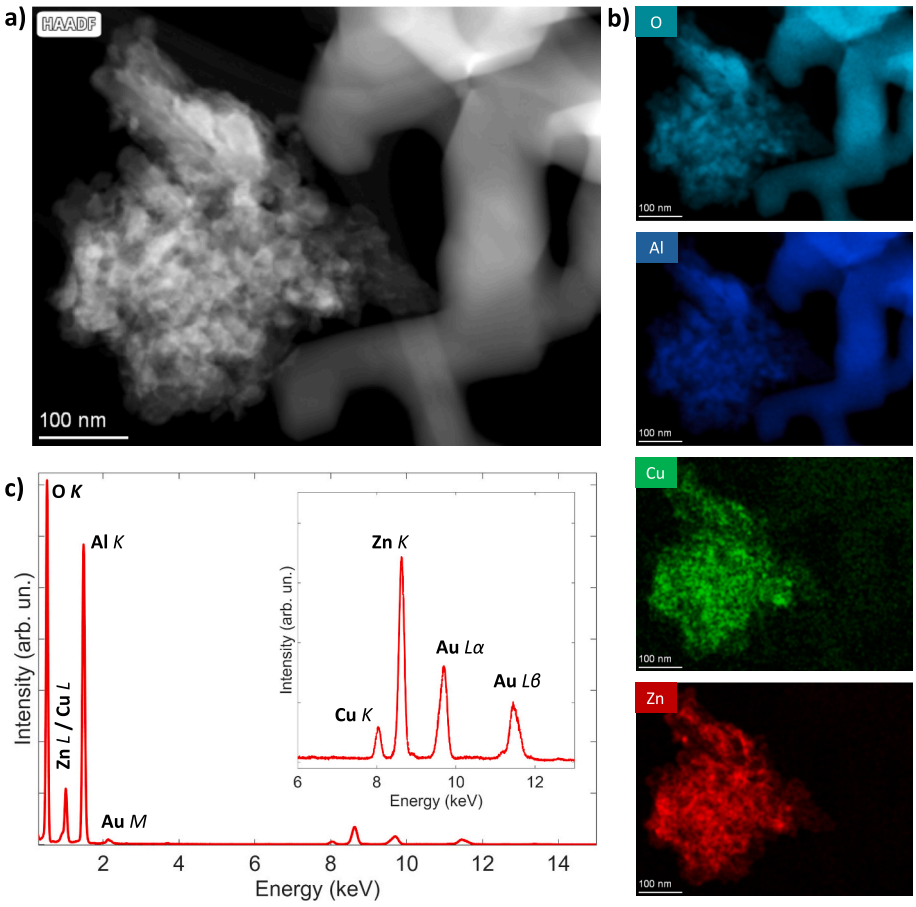

Fig. 9. High-angle annular dark field (HAADF) STEM image of the CZA_nitrate sample, alongside the corresponding EDX maps for O, Al, Cu and Zn. The sum spectrum is provided in c). The Au signal is due to the TEM grid.

for each catalyst, the CO_2 hydrogenation reaction was performed at 180, 200, 250, 300, and 350 °C. The three prepared catalysts were compared in terms of methanol selectivity (S_{MeOH}) and methanol TOF. Fig. 10 presents the methanol selectivity results at different WHSV and reaction temperatures.

The data reveal that selectivity is strongly influenced by temperature but remains largely unaffected by WHSV. Across all WHSV values, the catalysts exhibit high S_{MeOH} (~100 %) at lower temperatures (180 °C and 200 °C). However, at temperatures above 200 °C, S_{MeOH} declines sharply, approaching 0 % at 300 °C and 350 °C. This trend is further confirmed in Fig. 11, which provides a more detailed breakdown of the selectivity towards methanol, methane, and CO as a function of temperature at WHSV = 10 h^{-1}.

All catalysts display a similar selectivity pattern, where S_{MeOH} remains high (~100 %) up to 200 °C, then starts to decline as temperature increases. Simultaneously, CO selectivity rises, becoming the dominant product at temperatures above 250 °C, reaching nearly 100 % selectivity at 300 °C and beyond. The formation of methane remains negligible for all catalysts across the tested temperature range, indicating that the decline in S_{MeOH} is primarily due to CO formation [66]. Therefore, the system is not solely governed by CO_2 hydrogenation to methanol (reaction R1) but also by the reverse water-gas shift (RWGS) reaction (reaction R2), which becomes more prominent at higher temperatures.

$$CO_2 + 3H_2 \leftrightarrow CH_3OH + H_2O \quad \text{(R1)}$$

$$CO_2 + H_2 \leftrightarrow CO + H_2O \quad \text{(R2)}$$

This behavior is consistent with previous studies on Cu/ZnO/Al_2O_3 catalysts for CO_2 hydrogenation to methanol, where higher temperatures favor CO formation due to thermodynamic limitations on methanol synthesis [17,67]. Importantly, since all three catalysts exhibit a similar trend, it can be concluded that the choice of precursor salts does not significantly affect the selectivity profile under atmospheric pressure conditions.

The differences in catalytic performance for methanol synthesis become more evident when analyzing methanol TOF, as shown in Fig. 12. TOF is a crucial parameter as it provides a more comprehensive evaluation of catalyst efficiency. Fig. 12 presents methanol TOF as a function of both WHSV and temperature, highlighting distinct trends among the prepared catalysts.

Methanol TOF follows a consistent trend across all tests, with methanol TOF increasing with temperature and reaching its maximum at 250 °C. However, as depicted in Fig. 11, while TOF peaks at 250 °C, methanol selectivity is significantly reduced. Among the catalysts, CZA_nitrate consistently exhibits the highest TOF at all WHSV values, reinforcing its superior catalytic performance. The significantly higher TOF observed for CZA_nitrate compared to CZA_acetate and CZA_-chloride suggests that the enhanced Cu/ZnO interface, as discussed in the TPR and Raman analysis, plays a key role in promoting CO_2 hydrogenation to methanol. In contrast, CZA_chloride shows the lowest productivity, further confirming that the presence of $CuAl_2O_4$ limits the availability of active Cu sites.

This correlation between methanol productivity and the Cu/ZnO interface is further supported by Fig. 13, which presents the trend of productivity as a function of $Cu_{interface}$ content.

The data reveal a strong linear correlation between methanol productivity and the amount of Cu at the Cu/ZnO interface, with high correlation coefficients (R^2) for all tested WHSV values. This trend confirms that the Cu/ZnO interface plays a crucial role in determining methanol productivity, further justifying the superior performance of CZA_nitrate, which exhibits the highest $Cu_{interface}$ content (Table 2). This finding strongly supports that the Cu/ZnO interface constitutes the

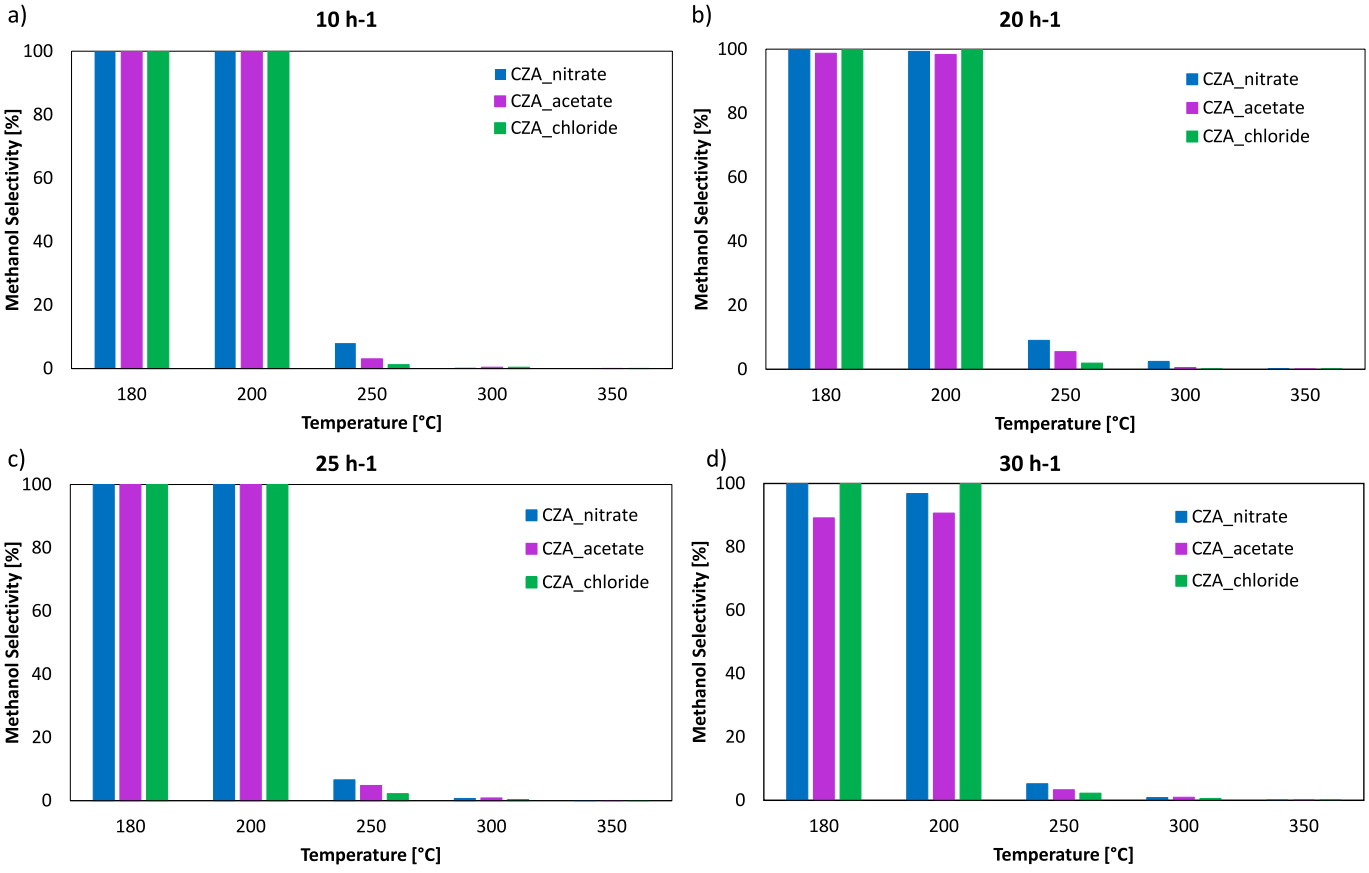

Fig. 10. Methanol selectivity at atmospheric pressure for the three catalysts (CZA_nitrate, CZA_acetate, and CZA_chloride) at different temperatures and WHSV values. The results are shown for (a) 10 h^{-1}, (b) 20 h^{-1}, (c) 25 h^{-1}, and (d) 30 h^{-1}.

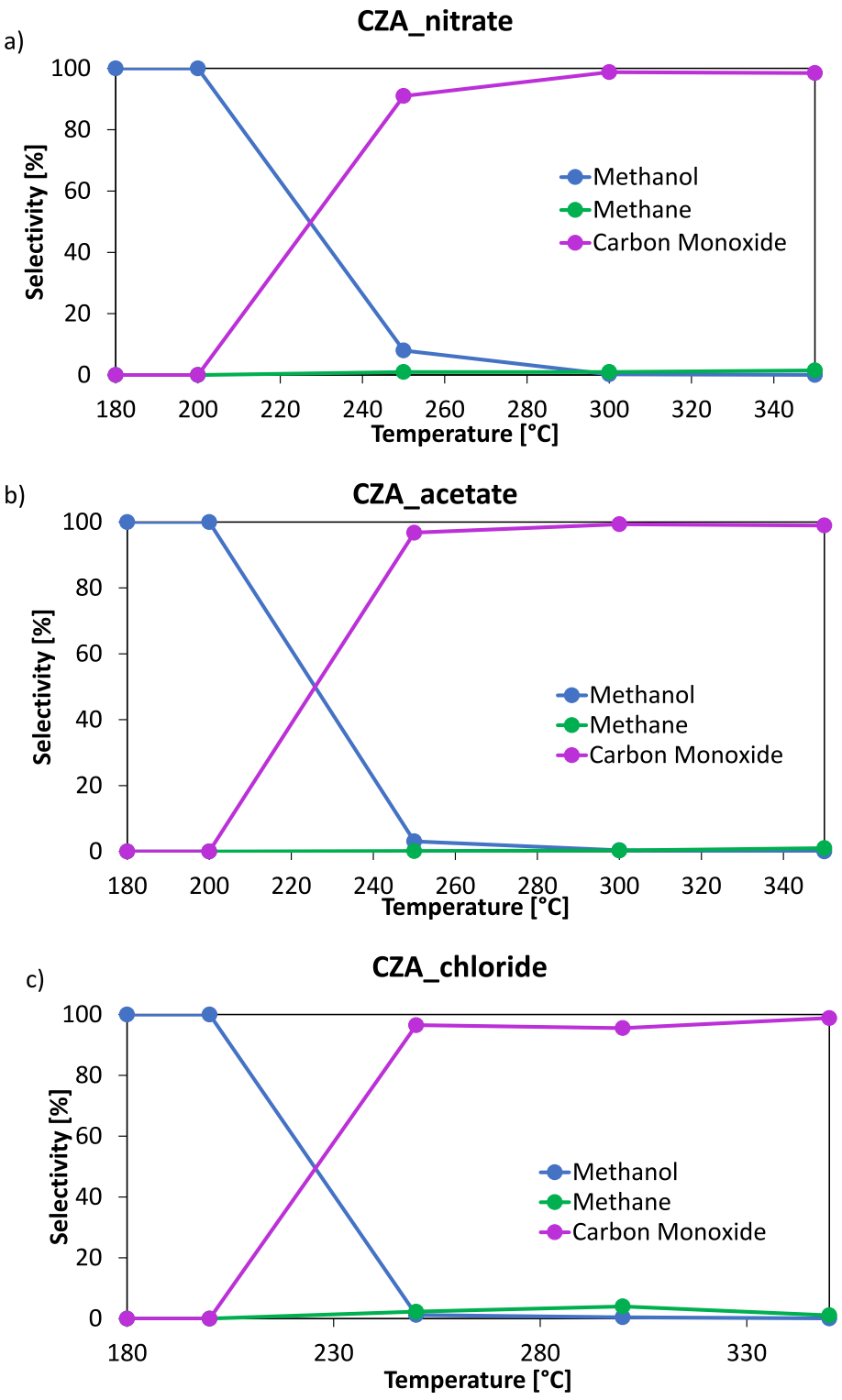

Fig. 11. Selectivity trends of methanol, methane, and carbon monoxide as a function of reaction temperature for the three catalysts: (a) CZA_nitrate, (b) CZA_acetate, and (c) CZA_chloride at WHSV = 10 h^{-1} and atmospheric pressure.

primary active site for CO_2 hydrogenation to methanol. The slope of the linear fit can be interpreted as a measure of intrinsic catalytic activity per mole of interfacial Cu, highlighting the critical importance of interfacial engineering in catalyst design. This correlation not only validates the TPR-based quantification approach but also confirms that the observed catalytic behavior is directly linked to the physicochemical properties induced by the choice of precursor salts.

A comprehensive analysis of the catalytic performance indicates that an optimal set of operating conditions can be identified to balance methanol productivity and selectivity. The results demonstrate that S_{MeOH} remains near 100 % at 180 °C and 200 °C, ensuring minimal by-products formation. However, at 200 °C, TOF is significantly higher compared to 180 °C, making this temperature more favorable for efficient CO_2 hydrogenation. Furthermore, among the tested WHSV values,

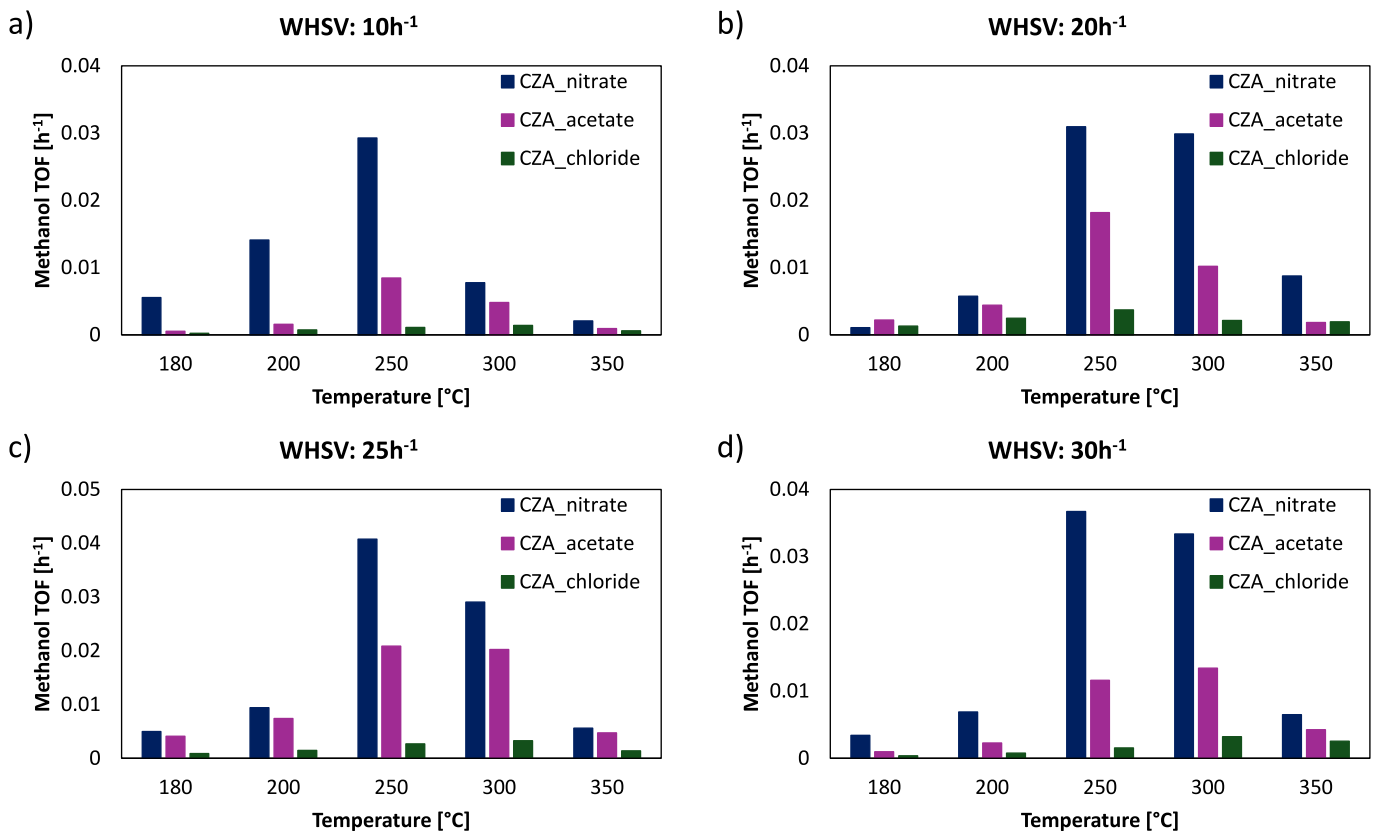

Fig. 12. Methanol TOF at atmospheric pressure and different temperatures for varying Weight Hourly Space Velocity (WHSV) values: (a) 10 h^{-1}, (b) 20 h^{-1}, (c) 25 h^{-1}, and (d) 30 h^{-1}.

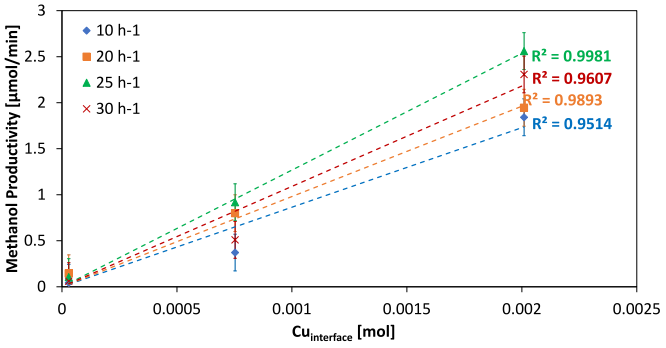

Fig. 13. Correlation between methanol productivity and the $Cu_{interface}$ content for different Weight Hourly Space Velocity (WHSV) values at 250 °C and atmospheric pressure.

the highest productivity is achieved at 10 h^{-1}, indicating that a lower space velocity enhances the contact time between reactants and active sites, promoting higher methanol yields. Consequently, under atmospheric pressure conditions, 200 °C and a WHSV of 10 h^{-1} emerge as the most effective parameters for maximizing methanol production while maintaining high selectivity.

Therefore, stability tests (Fig. 14) were performed under these optimized conditions (200 °C and WHSV of 10 h^{-1}) to assess the long-term performance of the catalysts. The evaluation focused on both S_{MeOH} (Fig. 14a) and methanol productivity (Fig. 14b) over an extended reaction period, providing insights into catalyst stability and deactivation phenomena.

The results reveal distinct trends among the catalysts. Both CZA_nitrate and CZA_acetate exhibit stable S_{MeOH} over the 10 h testing period, with no significant fluctuations (Fig. 14a). However, CZA_chloride shows a slight decline in selectivity (Fig. 14a), which may indicate a progressive deactivation mechanism that could become more pronounced over longer reaction times. In terms of methanol productivity (Fig. 14b), CZA_nitrate consistently outperforms the other samples, maintaining the highest productivity levels. CZA_acetate follows a stable trend but at a lower rate compared to CZA_nitrate. On the other hand, CZA_chloride exhibits a gradual decrease in productivity (Fig. 14b), suggesting that deactivation phenomena are occurring during the reaction. This decline in performance necessitated further investigation into potential deactivation mechanisms. To assess whether coke deposition contributed to catalyst deactivation, post-reaction temperature-programmed oxidation (TPO) analysis was performed (Fig. 15).

The comparison between CZA_nitrate and CZA_chloride indicates that CO_2 evolution is only observed for the CZA_chloride sample during the oxidation step, confirming the presence of coke deposits. This carbonaceous buildup can be directly linked to the observed decrease in both S_{MeOH} and productivity over time for CZA_chloride (Fig. 14). The presence of coke deposits in CZA_chloride can be correlated with the formation of Cu—Al spinel-like phases, which were detected in this sample (see XRD, Raman and H_2-TPR results) and are known to influence catalyst deactivation. Several studies report that aluminates can contribute to carbon deposition [68–70], leading to progressive deactivation. Unlike the other catalysts, where Cu is mainly present in highly dispersed or interface phases, the presence of Cu—Al interactions in CZA_chloride likely modifies the catalyst surface properties, favoring side reactions that result in coke formation. This explains the decline in both S_{MeOH} and productivity during the reaction time.

To further validate the durability of the most promising formulation, an extended 72-h stability test was conducted on the CZA_nitrate catalyst under the optimal operating conditions (200 °C, 1 bar, WHSV = 10 h^{-1}). As shown in Fig. 16, methanol productivity and selectivity

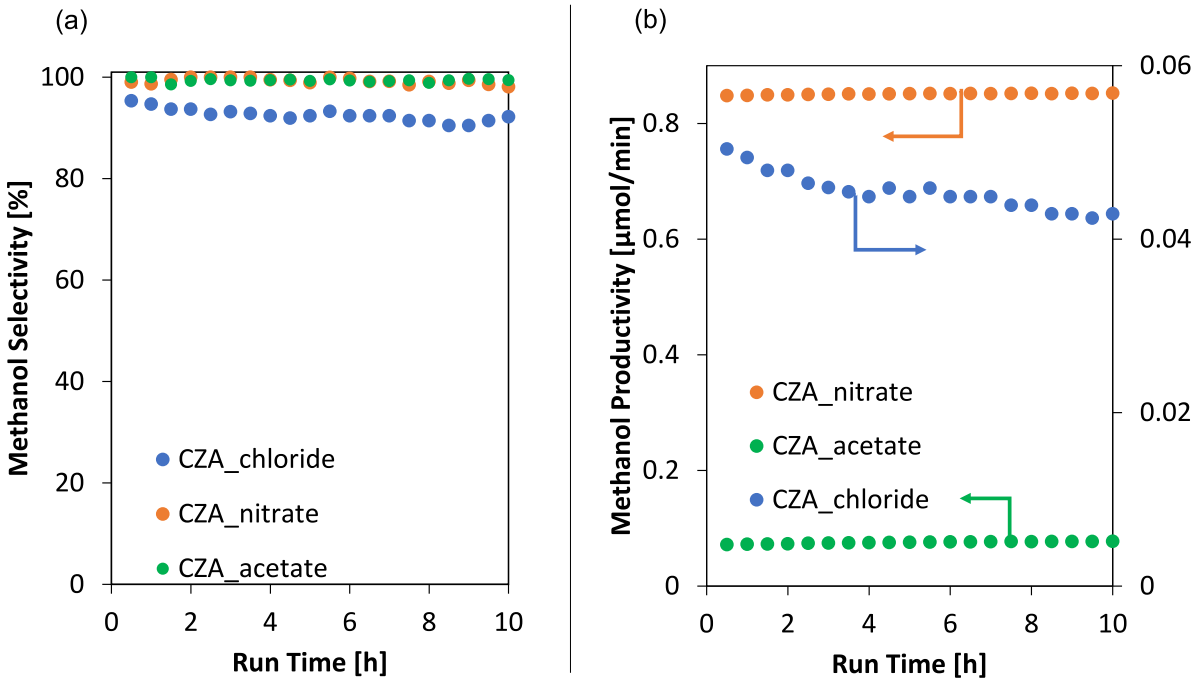

Fig. 14. Stability tests results for CZA_nitrate, CZA_acetate, and CZA_chloride at atmospheric pressure, WHSV 10 h^{-1}, and 200 °C.

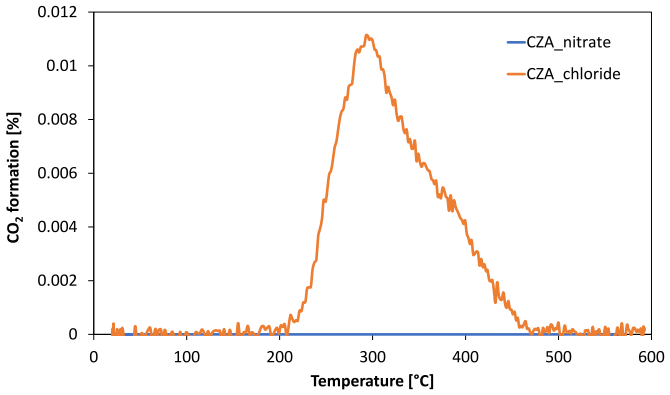

Fig. 15. CO_2 formation during post-reaction TPO for CZA_nitrate and CZA_chloride.

remained stable throughout the entire test period. Specifically, methanol productivity was consistently maintained at ~0.085 µmol/min, while methanol selectivity remained close to 100 %, confirming the excellent long-term performance and resistance to deactivation of the CZA_nitrate catalyst under mild conditions. It is important to note that during CO_2 hydrogenation, every mole of CO_2 converted to methanol or CO inherently generates 1 mol of H_2O, creating hydrothermal conditions inside the reactor. Previous studies have highlighted that such conditions often compromise the durability of commercial Cu/ZnO/Al_2O_3 catalysts [71]. In this context, the stable performance of CZA_nitrate over 72 h of continuous operation (Fig. 16) is particularly significant, as it implies that the Cu–ZnO interface in this formulation is less prone to hydrothermal degradation. This enhanced interfacial stability further strengthens the role of nitrate-derived precursors in promoting durable Cu–ZnO interactions under reaction conditions.

Following the confirmation of long-term stability under optimal reaction conditions (200 °C, 1 bar, WHSV = 10 h^{-1}) over 72 h, the performance of the CZA_nitrate catalyst was further evaluated by direct comparison with a commercial Cu/ZnO/Al_2O_3 catalyst (CZA_commercial, supplied by ThermoFisher Scientific), as presented in Fig. 17.

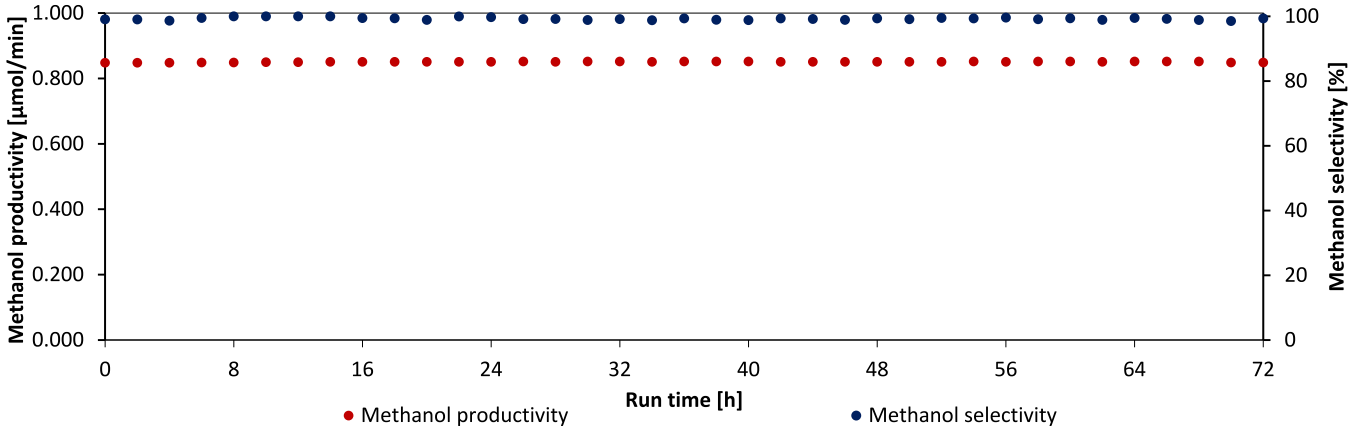

Fig. 16. Long-term stability test of the CZA_nitrate catalyst performed at 200 °C, 1 bar, and WHSV = 10 h^{-1} over 72 h.

The results clearly demonstrate that CZA_nitrate achieves 100 % methanol selectivity, whereas CZA_commercial reaches only 23 %. This indicates that CZA_nitrate strongly favors methanol formation, effectively suppressing undesired side reactions. The superior selectivity of CZA_nitrate suggests that the Cu/ZnO interface in this catalyst is highly optimized for CO_2 hydrogenation, favoring the selective conversion to methanol while minimizing RWGS reaction. Conversely, the lower selectivity observed for CZA_commercial implies a significant contribution from side reactions, leading to by-product formation, likely including CO via the RWGS reaction. This behavior might be attributed to differences in metal dispersion and Cu/ZnO interfacial properties, which strongly influence the reaction mechanism.

To further evaluate the performance of the CZA_nitrate catalyst, its methanol selectivity was compared with data from some previous studies on CO_2 hydrogenation to methanol at atmospheric pressure (Table 4).

The CZA_nitrate catalyst exhibits outstanding performance, achieving 100 % S_{MeOH} at 180 °C and 200 °C under atmospheric pressure. These results emphasize its superiority compared to previously reported $Cu/ZnO/Al_2O_3$-based and Pd-based catalysts, which generally exhibit lower S_{MeOH} under comparable conditions. While the La_2O_3-promoted $CuO/ZnO/Al_2O_3$ catalyst [25] also achieves 100 % S_{MeOH}, this occurs only at 160 °C. However, its performance declines significantly with increasing temperature, dropping to 70 % at 190 °C, 40 % at 210 °C, and just 5 % at 240 °C. This trend suggests that side reactions, such as the RWGS reaction, become dominant at higher temperatures, limiting its operational range at atmospheric pressure. In contrast, CZA_nitrate maintains 100 % selectivity up to 200 °C, a temperature more favorable for methanol production due to higher reaction rates, while at 250 °C, it still retains 10 % methanol selectivity. This is significantly better than the La-promoted catalyst, which rapidly loses its selectivity beyond 190 °C under atmospheric conditions. The Pd-based catalysts [72] show even lower methanol selectivity: 65.1 % for Pd/ZnO, 23.3 % for Pd/Ga_2O_3, and 30.4 % for Cu/ZnO at 190 °C under atmospheric pressure.

To further contextualize the catalytic performance of the CZA_nitrate sample, methanol TOF values were calculated (Table 6). Although CZA_nitrate exhibits lower TOF values than some Pd-based systems (e.g., Pd/ZnO with TOF ~4 h^{-1}), it consistently delivers 100 % methanol selectivity at 180–200 °C under 1 bar, a performance not matched by other catalysts operating at comparable conditions. Notably, some of the Pd-based catalysts achieving higher TOF do so at the expense of selectivity. We believe that in methanol synthesis via CO_2 hydrogenation, selectivity is a key metric, especially for downstream purification and process efficiency. This result highlights the CZA_nitrate catalyst to direct the reaction pathway towards methanol formation while suppressing competing side reactions.

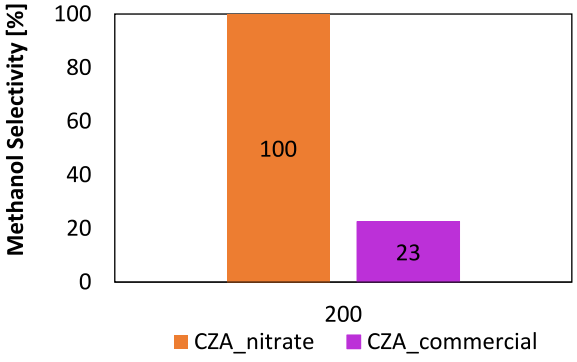

Fig. 17. Methanol selectivity at WHSV 10 h^{-1}, 200 °C, and 1 bar for CZA_nitrate and CZA_commercial.

Table 6
Comparison between methanol selectivity in the present work and in literature at atmospheric pressure.

Reference	Catalyst	Temperature [°C]	Methanol selectivity [%]	TOF [h^{-1}]
Present work	CZA_nitrate	180	100	0.0556
		200	100	0.0141
		250	10	0.02929
[25]	La_2O_3-promoted $CuO/ZnO/Al_2O_3$	160	100	/
		190	70	/
		210	40	/
		240	5	/
[72]	Pd/ZnO	190	65.1	3.96
	Pd/Ga_2O_3	190	23.3	0.432
	Cu/ZnO	190	30.4	0.27

3.2.2. *Effect of pressure on methanol synthesis performance*

Methanol synthesis from CO_2 and H_2 is limited by thermodynamic equilibrium, especially under atmospheric pressure and at elevated temperatures, where the RWGS reaction becomes increasingly favored. At 1 bar, the equilibrium conversion is intrinsically low, restricting the overall methanol yield even in the presence of active and selective catalysts. To overcome this limitation, additional catalytic tests were performed using the best-performing catalyst (CZA_nitrate) at elevated pressures up to 7 bar. In particular, CO_2 hydrogenation tests were conducted at elevated pressures (up to 7 bar) while maintaining a constant WHSV of 10 h^{-1} and varying the reaction temperature (Figs. 18 and 19).

The results reveal a strong dependence of CO_2 conversion, methanol selectivity, and methanol productivity on operating pressure. As shown in Fig. 18a, CO_2 conversion remains low at 1 bar, regardless of the temperature. However, increasing the pressure to 4 bar leads to a noticeable rise in CO_2 conversion (7 % at 350 °C). At 7 bar, a significant increase in CO_2 conversion is observed, reaching approximately 23 % at 350 °C. S_{MeOH} (Fig. 18b) follows the expected trend, with high selectivity at low temperatures (180–200 °C) across all pressures. However, at higher temperatures, S_{MeOH} decreases due to the promotion of competing reactions, particularly the RWGS reaction. Notably, increasing the pressure to 7 bar mitigates this selectivity drop, extending the range of high S_{MeOH} to slightly higher temperatures compared to 1 bar and 4 bar. This effect is primarily linked to the thermodynamic equilibrium of methanol synthesis, which is favored at higher pressures, as methanol formation involves a net reduction in the total number of gas-phase molecules. Consequently, increasing pressure enhances methanol yield while suppressing the direct hydrogenation of CO_2 to CO via the RWGS pathway [73]. Moreover, the kinetic barrier for methanol synthesis is reduced at higher pressures, allowing for greater methanol productivity while limiting undesirable side reactions [74]. Indeed, TOF (Fig. 18c) exhibits a pressure-dependent maximum, peaking at 250 °C for all conditions. At 1 bar, TOF is significantly lower than at 4 and 7 bar, reflecting the lower CO_2 conversion. At 7 bar, the maximum TOF surpasses 0.5 h^{-1} (30 μmol/min), demonstrating the positive impact of higher pressure on methanol formation rate.

The detailed product distribution analysis in Fig. 19 further supports these observations.

At 1 bar (Fig. 19a), methanol is the dominant product at low temperatures, but selectivity declines rapidly above 200 °C, with CO becoming the main product due to RWGS. The formation of methane remains negligible. At 4 bar (Fig. 19b), CO formation is still dominant at high temperatures, but S_{MeOH} remains high over a broader range. At 7 bar (Fig. 19c), S_{MeOH} remains high at lower temperatures (180–200 °C), similar to the trends observed at lower pressures. Notably, at 250 °C, S_{MeOH} at 7 bar (about 50 %) is higher than at 4 bar (about 30 %), suggesting that increased pressure helps to suppress side reactions, maintaining a more favorable environment for methanol synthesis at this temperature. Regarding CO selectivity, the data reveal that increasing the pressure to 7 bar significantly suppresses CO formation at lower

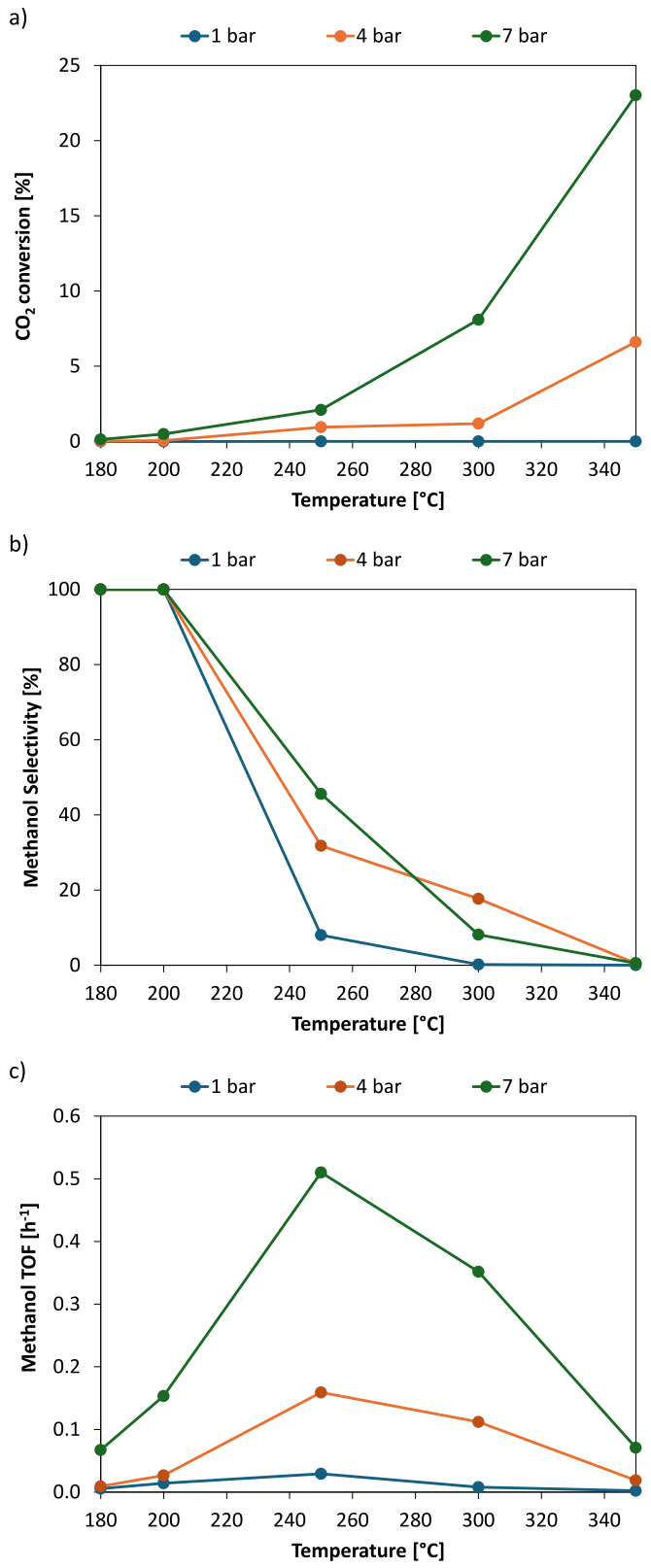

Fig. 18. High-pressure test results for CZA_nitrate at WHSV 10 h^{-1}, 200 °C, and different pressures (1, 4, and 7 bar) showing: (a) CO_2 conversion, (b) methanol selectivity, and (c) methanol productivity.

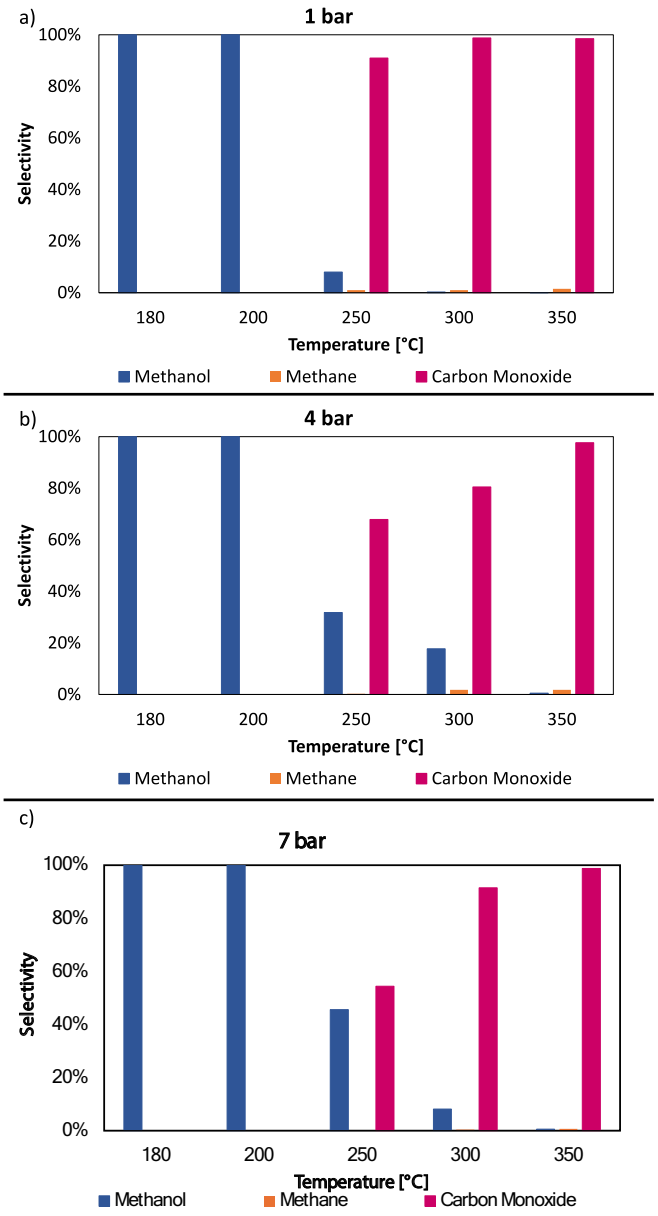

Fig. 19. Selectivity to methanol, methane, and carbon monoxide at WHSV 10 h^{-1}, under different temperatures and pressures: (a) 1 bar, (b) 4 bar, and (c) 7 bar.

temperatures. While at 1 bar and 4 bar, CO production becomes dominant beyond 250 °C, at 7 bar, the increase in CO selectivity is delayed, appearing more prominently only at 300 °C and higher. Finally, methane formation remains minimal across the entire temperature and pressure range, with its extent still negligible compared to CO production, confirming that the only significant side reaction under the investigated operating conditions is the RWGS reaction.

To evaluate the consistency between experimental data and thermodynamic limitations, methanol selectivity under equilibrium conditions was calculated using the Gaseq software (version 0.79). The model considered only the main reactions relevant under the tested conditions: CO_2 hydrogenation to methanol and the reverse water–gas shift (RWGS) reaction.

The comparison between experimental and calculated equilibrium methanol selectivity (Table S1) revealed a marked deviation at low temperatures. For instance, at 180 °C and 1 bar, the equilibrium selectivity was only 3.1 %, while the experimental value reached 100 %. A similar trend was observed at 200 °C. These discrepancies confirm that

under these mild conditions, the reaction is not limited by thermodynamics but is instead governed by kinetic factors. The high selectivity observed for the CZA_nitrate catalyst is thus attributed to its ability to promote methanol formation and inhibit the competing RWGS reaction.

In addition, to validate the reliability of the catalytic tests, a full carbon mass balance was performed for all experiments. Despite the challenges posed by the low conversion levels and the use of a highly sensitive detector (optimized for product quantification), the total carbon balance consistently closed within 98 ± 2 %. This high level of closure confirms the robustness and accuracy of the experimental methodology and supports the validity of the reported selectivity and productivity values.

Furthermore, a dedicated test at 30 bar and 200 °C confirmed this trend: the CZA_nitrate catalyst achieved 14 % CO_2 conversion and 90 % methanol selectivity, demonstrating its potential under industrially relevant conditions. These findings are consistent with previous reports. For instance, Gaikwad et al. [66] demonstrated that high pressure significantly enhances methanol productivity in CO_2 hydrogenation due to favorable thermodynamics. Compared to the Ga-promoted Cu/ZnO catalysts studied by Cored et al. [75] at similar temperature and lower pressure (20 bar, 200 °C), which achieved CO_2 conversions of 6.2 % and 4.9 % with selectivities of 90 % and 95 %, respectively, CZA_nitrates demonstrates a markedly higher activity while maintaining comparable selectivity. Furthermore, when compared to the Zr-promoted CZA catalyst investigated by Ren et al. [76] at higher pressure and temperature (60 bar, 260 °C), which showed a CO_2 conversion of 25 % and a methanol selectivity of 63 %, the CZA_nitrates catalyst offers a favorable balance of conversion and selectivity under milder conditions.

This confirms the crucial role of reaction pressure in overcoming equilibrium constraints and further validates the excellent performance of CZA_nitrate under both mild and pressurized conditions.

4. Industrial relevance and potential optimizations

Operating at moderate pressures (1–7 bar) and low temperatures (180–200 °C) offers a clear advantage in terms of reduced hydrogen/CO_2 compression work and simplified plant utilities. However, the thermodynamic limitation at low pressure yields low single-pass conversions and consequently larger reactor volumes and higher recycle/separation duties. Importantly, CZA_nitrate preserves excellent methanol selectivity when pressure is raised (e.g., ~14 % CO_2 conversion and ~ 90 % methanol selectivity at 30 bar, 200 °C), indicating suitability across a range of operating pressures. To translate the promising lab-scale selectivity into industrial competitiveness at moderate pressure, two complementary paths are envisaged: material-level improvements, increasing active Cu–ZnO interfacial density via high-surface-area or structured supports, promoter/dopant addition, and catalyst shaping (monoliths, washcoats) (aimed at increasing intrinsic activity and space-time yield); process-level innovations, staging with internal recycle, reaction–separation coupling (e.g., selective water removal or membrane reactors) or pressure-swing strategies to shift the equilibrium. Future work will quantify performance with industrially relevant metrics (Space-Time Yield (STY), and energy per kg MeOH) and will include a preliminary techno-economic assessment to compare compression energy savings against the penalties of larger reactors and separation duty.

5. Conclusions

This study highlights the crucial role of precursor salt selection in determining the physicochemical properties and catalytic performance of Cu/ZnO/Al_2O_3 (CZA) catalysts for CO_2 hydrogenation to methanol. By varying the Cu and ZnO precursor salts (nitrate, acetate, and chloride), significant differences were observed in Cu dispersion, metal-support interaction, and Cu phase distribution, which directly influenced catalytic activity and selectivity.

Among the prepared catalysts, CZA_nitrate exhibited the strongest Cu/ZnO interaction and the highest Cu species content at the ZnO interface, as evidenced by a prominent Cu^{2+}-ZnO charge transfer band in UV–Vis DRS and a higher Cu interface content derived from TPR peak deconvolution analysis. In contrast, CZA_chloride exhibited a significantly lower Cu-ZnO interface content and the presence of $CuAl_2O_4$ spinel-like species, as confirmed by Raman spectroscopy and XRD analysis, which hinder Cu-ZnO interactions.

CO_2 hydrogenation tests confirmed that CZA_nitrate exhibited superior catalytic performance, achieving 100 % methanol selectivity at 180–200 °C under atmospheric pressure, coupled with the highest methanol productivity. In addition to its superior selectivity and productivity, the CZA_nitrate catalyst also demonstrated remarkable stability under reaction conditions, which inherently involve hydrothermal stress due to water formation. The preservation of methanol selectivity and productivity over 72 h suggests that the Cu–ZnO interface in CZA_nitrate is highly resistant to hydrothermal degradation, a common limitation of commercial Cu/ZnO/Al_2O_3 catalysts.

Furthermore, methanol productivity was found to be strongly dependent on the Weight Hourly Space Velocity (WHSV). Among the tested conditions, the highest methanol productivity was achieved at 10 h^{-1} and 200 °C under 1 bar. A linear correlation between methanol productivity and the amount of Cu at the interface of ZnO was validated through quantitative TPR analysis, confirming that the Cu/ZnO interface is the key active site for CO_2 hydrogenation. The role of the Cu-ZnO interface was particularly evident when comparing CZA_nitrate and CZA_acetate, with the latter showing lower Cu interface content and reduced catalytic performance. Stability tests confirmed that CZA_nitrate retained its activity over prolonged reaction times, whereas CZA_chloride suffered from deactivation, attributed to coke formation, as evidenced by TPO analysis, likely promoted by the presence of $CuAl_2O_4$ species that inhibited Cu-ZnO interaction. This suggests that $CuAl_2O_4$ formation not only reduces Cu availability but also promotes carbon deposition, accelerating catalyst deactivation. At high pressures (up to 7 bar), methanol selectivity on CZA_nitrate remained high at lower temperatures, and at 250 °C, increasing the pressure mitigated RWGS side reactions, improving methanol selectivity from 10 % at 1 bar to approximately 30 % at 4 bar and 50 % at 7 bar. Notably, methane formation remained negligible across all tested conditions, confirming that RWGS was the only significant side reaction. Comparative testing against a commercial Cu/ZnO/Al_2O_3 catalyst further highlighted the superior selectivity of CZA_nitrate, demonstrating its high efficiency in methanol synthesis. Finally, a comparison with literature data confirmed that CZA_nitrate outperformed previously reported Cu-based catalysts at atmospheric pressure, achieving superior methanol selectivity even at low temperatures (180–200 °C). Although the present study highlights the importance of optimizing the Cu/ZnO interface to enhance catalytic performance and emphasizes the critical influence of precursor selection on catalyst design, further mechanistic insights are still needed. Future investigations should include in situ spectroscopic techniques such as DRIFTS to better elucidate the nature of active Cu species and surface intermediates during CO_2 hydrogenation over CZA_nitrate catalyst.

The combination of excellent selectivity at mild conditions and promising behavior at elevated pressure suggests that CZA_nitrate is a strong candidate for lower-temperature methanol synthesis. Its industrial attractiveness at moderate pressure will depend on material optimizations (support, promoters, structured catalysts) and process integrations (reaction–separation schemes); these avenues should be pursued in follow-up studies, alongside basic techno-economic comparisons using STY and energy per kg methanol as decision metrics.

However, this study provides valuable insights for the rational development of Cu-based catalysts for selective CO_2 conversion to methanol, offering potential avenues for improving catalyst stability, productivity, and selectivity through precursor engineering and controlled synthesis methods.

CRediT authorship contribution statement

Laura Chianese: Writing – original draft, Investigation, Data curation. **Rosanna Viscardi:** Visualization, Investigation. **Claudia Bassano:** Visualization. **Andrea Muscatello:** Investigation, Data curation. **Marco Fontana:** Formal analysis, Data curation. **Micaela Castellino:** Writing – original draft, Investigation, Formal analysis, Data curation. **Gianluca Landi:** Writing – original draft, Investigation, Data curation. **Stefano Scognamiglio:** Investigation, Data curation. **Serena Esposito:** Writing – review & editing, Supervision, Investigation, Conceptualization. **Vincenzo Palma:** Visualization, Resources. **Giuseppina Iervolino:** Writing – review & editing, Supervision, Conceptualization. **Vincenzo Vaiano:** Writing – review & editing, Supervision, Conceptualization.

Declaration of competing interest

The authors declare that they have no known competing financial interests or personal relationships that could have appeared to influence the work reported in this paper.

Appendix A. Supplementary data

Supplementary data to this article can be found online at https://doi.org/10.1016/j.cej.2025.169870.

Data availability

Data will be made available on request.

References

[1] L. Chianese, E. Meloni, V. Vaiano, G. Iervolino, V. Palma, Environmental Challenges and Economical Assessment of Methanol's Production Feedstock, 2024.
[2] M.M.-J. Li, S.C.E. Tsang, Bimetallic catalysts for green methanol production via CO 2 and renewable hydrogen: a mini-review and prospects, Technology 8 (14) (2018) 3450–3464.
[3] S. Kanuri, S. Roy, C. Chakraborty, S.P. Datta, S. Singh, S. Dinda, An insight of CO2 hydrogenation to methanol synthesis: thermodynamics, catalysts, operating parameters, and reaction mechanism 46 (5) (2022) 5503–5522.
[4] S. Sun, H. Sun, P.T. Williams, C.J.S.E. Wu, Recent advances in integrated CO2 capture and utilization: a review, Fuels 5 (18) (2021) 4546–4559.
[5] T. Biswal, K.P. Shadangi, P.K. Sarangi, R.K.J.C. Srivastava, Conversion of carbon dioxide to methanol: a comprehensive review 298 (2022) 134299.
[6] H. Lee, K. Calvin, D. Dasgupta, G. Krinner, A. Mukherji, P. Thorne, C. Trisos, J. Romero, P. Aldunce, K. Barrett, Climate Change 2023: Synthesis Report. Contribution of Working Groups I, II and III to the Sixth Assessment Report of the Intergovernmental Panel on Climate Change, The Australian National University, 2023.
[7] G.A. Olah, A. Goeppert, G.S. Prakash, Beyond Oil and Gas: the Methanol Economy, John Wiley & Sons, 2018.
[8] F. Dalena, A. Senatore, A. Marino, A. Gordano, M. Basile, A. Basile, Methanol production and applications: an overview, Methanol (2018) 3–28.
[9] V. Barbarossa, R. Viscardi, Utilizzo della CO_2 per produzione di combustibili, Catalysis Research (2015) 1–12.
[10] M. Bertau, H. Offermanns, L. Plass, F. Schmidt, H.-J. Wernicke, Methanol: the Basic Chemical and Energy Feedstock of the Future, Springer, 2014.
[11] M.J.C. Bowker, Methanol synthesis from CO_2 hydrogenation, ChemCatChem 11 (17) (2019) 4238–4246.
[12] I. Ganesh, Conversion of carbon dioxide into methanol–a potential liquid fuel: fundamental challenges and opportunities (a review), Renewable Sustainable Energy Reviews 31 (2014) 221–257.
[13] Y. Wang, L.R. Winter, J.G. Chen, B. Yan, CO_2 hydrogenation over heterogeneous catalysts at atmospheric pressure: from electronic properties to product selectivity, Green Chem. 23 (1) (2021) 249–267.
[14] S.G. Jadhav, P.D. Vaidya, B.M. Bhanage, J.B. Joshi, Catalytic carbon dioxide hydrogenation to methanol: a review of recent studies, Chem. Eng. Res. Des. 92 (11) (2014) 2557–2567.
[15] F. Samimi, M.R. Rahimpour, A. Shariati, Development of an efficient methanol production process for direct CO2 hydrogenation over a Cu/ZnO/Al_2O_3 catalyst, Catalysts 7 (11) (2017) 332.
[16] S. Saeidi, N.A.S. Amin, M.R. Rahimpour, Hydrogenation of CO_2 to value-added products—a review and potential future developments, J CO_2 Util 5 (2014) 66–81.
[17] E.L. Kunkes, F. Studt, F. Abild-Pedersen, R. Schlögl, M. Behrens, Hydrogenation of CO_2 to methanol and CO on cu/ZnO/Al_2O_3: is there a common intermediate or not? J. Catal. 328 (2015) 43–48.
[18] H. Yan, D. Li, Z. Jiang, H. Gu, M. Zhu, Y.-F. Han, M. Zhu, Promotion of Cu/ZnO/Al2O3 by Fe towards methanol steam reforming reaction, Applied Catalysis B: Environment and Energy 365 (2025) 124984.
[19] X. Cui, Y. Liu, W. Yan, Y. Xue, Y. Mei, J. Li, X. Gao, H. Zhang, S. Zhu, Y. Niu, T. Deng, Enhancing methanol selectivity of commercial Cu/ZnO/Al_2O_3 catalyst in CO_2 hydrogenation by surface silylation, Appl. Catal. Environ. 339 (2023) 123099.
[20] S.D. Jones, H.E. Hagelin-Weaver, Steam reforming of methanol over CeO_2- and ZrO_2-promoted cu-ZnO catalysts supported on nanoparticle Al_2O_3, Appl. Catal. Environ. 90 (1) (2009) 195–204.
[21] J. Toyir, P.R. de la Piscina, N. Homs, Ga-promoted copper-based catalysts highly selective for methanol steam reforming to hydrogen; relation with the hydrogenation of CO_2 to methanol, Int. J. Hydrogen Energy 40 (34) (2015) 11261–11266.
[22] J. Toyir, P.R. De la Piscina, J.L.G. Fierro, N.s., Homs, catalytic performance for CO_2 conversion to methanol of gallium-promoted copper-based catalysts: influence of metallic precursors, Appl. Catal. Environ. 34 (4) (2001) 255–266.
[23] M. Behrens, F. Studt, I. Kasatkin, S. Kühl, M. Hävecker, F. Abild-Pedersen, S. Zander, F. Girgsdies, P. Kurr, B.L. Kniep, M. Tovar, R.W. Fischer, J.K. Nørskov, R. Schlögl, The active site of methanol synthesis over cu/ZnO/Al_2O_3 industrial catalysts, Science (New York, N.Y.) 336 (6083) (2012) 893–897.
[24] F. Chen, J. Liang, F. Wang, X. Guo, W. Gao, Y. Kugue, Y. He, G. Yang, P. Reubroycharoen, T. Vitidsant, Improved catalytic activity and stability of cu/ZnO catalyst by boron oxide modification for low-temperature methanol synthesis, Chem. Eng. J. 458 (2023) 141401.
[25] K.K.M. Kourtelesis, D.I. Kondarides, CO2 hydrogenation to methanol over La_2O_3-promoted CuO/ZnO/Al_2O_3 catalysts: a kinetic and mechanistic study, Catalysts 10 (2020) 183.
[26] M. Kipnis, E. Volnina, I. Belostotsky, R. Galkin, N. Zhilyaeva, I. Levin, S. Kottsov, A. Ezhov, Effective cu/ZnO/Al_2O_3 catalyst for methanol production: synthesis, activation, catalytic performance, and regeneration, Catalysis Research 2 (3) (2022) 1–20.
[27] N. Phongprueksathat, A. Bansode, T. Toyao, A. Urakawa, Greener and facile synthesis of cu/ZnO catalysts for CO_2 hydrogenation to methanol by urea hydrolysis of acetates, RSC Adv. 11 (24) (2021) 14323–14333.
[28] M. Behrens, D. Brennecke, F. Girgsdies, S. Kißner, A. Trunschke, N. Nasrudin, S. Zakaria, N.F. Idris, S.B. Abd Hamid, B. Kniep, Understanding the complexity of a catalyst synthesis: co-precipitation of mixed cu, Zn, Al hydroxycarbonate precursors for cu/ZnO/Al_2O_3 catalysts investigated by titration experiments, Appl. Catal. Gen. 392 (1–2) (2011) 93–102.
[29] S. Lee, K. Schneider, J. Schumann, A.K. Mogalicherla, P. Pfeifer, R. Dittmeyer, Effect of metal precursor on cu/ZnO/Al_2O_3 synthesized by flame spray pyrolysis for direct DME production, Chem. Eng. Sci. 138 (2015) 194–202.
[30] J. Chen, Y. He, C. Tang, J. Wang, Y. Sun, X. Wen, Z. Zhang, Zinc oxide morphology-dependent CuOx-ZnO interactions and catalysis in CO oxidation and CO2 hydrogenation, Appl. Surf. Sci. 680 (2025) 161295.
[31] X. Chang, X. Zi, J. Li, F. Liu, X. Han, J. Chen, Z. Hao, H. Zhang, Z. Zhang, P.J. C. Gao, An insight into synergistic metal-oxide interaction in CO2 hydrogenation to methanol over Cu/ZnO/ZrO2, J. Catal. 13 (10) (2023) 1337.
[32] W. Wang, Q. Zhou, X. Fei, Y. He, P. Zhang, G. Zhang, L. Peng, W. Xie, Synthesis of CuO nano-and micro-structures and their Raman spectroscopic studies, CrystEngComm 12 (7) (2010) 2232–2237.
[33] K.G. Krishna, S.R. Parne, P. Nagaraju, An optical study of heterojunction n-ZnO/p-CuO nanosheets and detection of n-butanol vapour at room temperature, J. Mater. Sci. 58 (40) (2023) 15660–15675.
[34] J. Fang, Y.J.R.a. Xuan, Investigation of optical absorption and photothermal conversion characteristics of binary CuO/ZnO nanofluids 7 (88) (2017) 56023–56033.
[35] M. Russo, G. Iervolino, V. Vaiano, W-doped zno photocatalyst for the degradation of glyphosate in aqueous solution, Catalysts 11 (2) (2021) 234.
[36] S. Kuriakose, B. Satpati, S. Mohapatra, Highly efficient photocatalytic degradation of organic dyes by Cu doped ZnO nanostructures, Phys. Chem. Chem. Phys. 17 (38) (2015) 25172–25181.
[37] B. Khalfallah, I. Riahi, F. Chaabouni, Effect of Cu doping on the structural, optical and electrical properties of ZnO thin films grown by RF magnetron sputtering: application to solar photocatalysis, Optical Quantum Electronics 53 (5) (2021) 238.
[38] K. Mubeen, A. Irshad, A. Safeen, U. Aziz, K. Safeen, T. Ghani, K. Khan, Z. Ali, I. ul Haq, A. Shah, Band structure tuning of ZnO/CuO composites for enhanced photocatalytic activity, J. Saudi Chem. Soc. 27 (3) (2023) 101639.
[39] B. Mavrin, L. Demyanets, R. Zakalukin, Raman spectroscopy and Fermi resonance in Mn-doped ZnO bulk single crystal, Phys. Lett. A 374 (39) (2010) 4054–4056.
[40] M. Soosen Samuel, J. Koshy, A. Chandran, K. George, Optical phonon confinement in ZnO nanorods and nanotubes, Indian J. Pure Appl. Phys. 48 (2010) 703–708.
[41] Y. Lv, H. Yan, T. Liu, J. Xu, X. Xu, X. Fang, X. Wang, Manufacturing AAl_2O_4 (A = Cu, Co, Ni, Zn) spinel catalysts for toluene combustion: elucidating the A-site replacement effect on the reactivity, ChemCatChem 16 (8) (2024) e202301264.
[42] V. Kumari, S. Yadav, J. Jindal, S. Sharma, K. Kumari, N. Kumar, Synthesis and characterization of heterogeneous ZnO/CuO hierarchical nanostructures for photocatalytic degradation of organic pollutant, Adv. Powder Technol. 31 (7) (2020) 2658–2668.
[43] S. Yashnik, M. Kerzhentsev, A. Salnikov, Z. Ismagilov, A. Bourane, O. Koseoglu, Cu-Zn-Al-O catalysts for the oxidative desulfurization of dibenzothiophene, a typical sulfur-containing compound of the diesel fraction, Kinetics Catalysis 56 (2015) 466–475.
[44] N. Morante, O. Tammaro, K. Monzillo, D. Sannino, A. Battiato, E. Vittone, M. Castellino, S. Esposito, V. Vaiano, Unraveling the role of CuO in CuxO/TiO2

photocatalyst for the direct propylene epoxidation with O2 in a fluidized bed reactor, ChemSusChem 18 (2025) e202401546 (1-16).
[45] A. Le Nestour, M. Gaudon, G. Villeneuve, M. Daturi, R. Andriessen, A. Demourgues, Defects in divided zinc– copper aluminate spinels: structural features and optical absorption properties, Inorg. Chem. 46 (10) (2007) 4067–4078.
[46] K. Stangeland, H.H. Navarro, H.L. Huynh, W.M. Tucho, Z. Yu, Tuning the interfacial sites between copper and metal oxides (Zn, Zr, In) for CO_2 hydrogenation to methanol, Chem. Eng. Sci. 238 (2021) 116603.
[47] Y. Sun, C. Huang, L. Chen, Y. Zhang, M. Fu, J. Wu, D. Ye, Active site structure study of Cu/plate ZnO model catalysts for CO2 hydrogenation to methanol under the real reaction conditions, J CO_2 Util 37 (2020) 55–64.
[48] M.-F. Luo, P. Fang, M. He, Y.-L. Xie, In situ XRD, Raman, and TPR studies of CuO/Al2O3 catalysts for CO oxidation, J. Mol. Catal. A Chem. 239 (1–2) (2005) 243–248.
[49] V.D. Dasireddy, S.Š. Neja, L. Blaž, Correlation between synthesis pH, structure and Cu/MgO/Al2O3 heterogeneous catalyst activity and selectivity in CO2 hydrogenation to methanol, J CO_2 Util 28 (2018) 189–199.
[50] X. Wei, W.G. Su, Y. Shi, J. Wang, P. Lv, X. Song, Y. Bai, G. Xu, G. Yu, Cu0 at the Cu/ZnO interface efficiently accelerate CO2 hydrogenation to methanol over Cu/ZnO/C–P catalysts, Int. J. Hydrogen Energy 58 (2024) 128–136.
[51] W.-P. Dow, Y.-P. Wang, T.-J. Huang, TPR and XRD studies of yttria-doped ceria/γ-alumina-supported copper oxide catalyst, Appl. Catal. Gen. 190 (1–2) (2000) 25–34.
[52] F. Zhang, Y. Liu, X. Xu, P. Yang, P. Miao, Y. Zhang, Q. Sun, Effect of Al-containing precursors on Cu/ZnO/Al2O3 catalyst for methanol production, Fuel Process. Technol. 178 (2018) 148–155.
[53] A.T. Mohamed, Y.H. Ahmad, A.H. Anwer, A. Soliman, M.A.H. Saad, M.K. Aroua, S. Y. Al-Qaradawi, A. Benamor, CO2 conversion to dimethyl ether on cu/ZnO/Al2O3-ZSM-5 tandem catalysts in a double-bed reactor: tuning the ZSM-5 catalyst acidity and porosity, Energy & Fuels 39 (4) (2025) 2059–2074.
[54] M. Nagai, K. Koizumi, S. Omi, NH3-TPD and XPS studies of Ru/Al2O3 catalyst and HDS activity, Catal. Today 35 (4) (1997) 393–405.
[55] Z. Liu, X. An, M. Song, Z. Wang, Y. Wei, S. Mintova, G. Giordano, Z. Yan, Dry gel assisting crystallization of bifunctional CuO–ZnO–Al2O3/SiO2–Al2O3 catalysts for CO2 hydrogenation, Biomass Bioenergy 163 (2022) 106525.
[56] M. Li, L. Jiao, M.A. Nawaz, L. Cheng, C. Meng, T. Yang, M. Tariq, D. Liu, A one-step synthesis method of durene directly from syngas using integrated catalyst of Cu/ZnO/Al2O3 and Co-Nb/HZSM-5, Chem. Eng. Sci. 200 (2019) 103–112.
[57] E. Catizzone, G. Bonura, M. Migliori, G. Braccio, F. Frusteri, G. Giordano, Direct CO 2-to-dimethyl ether hydrogenation over CuZnZr/zeolite hybrid catalyst: new evidences on the interaction between acid and metal sites, Annales de Chimie Science des Matériaux 43 (3) (2019) 141–149.
[58] O. Tursunov, L. Kustov, Z. Tilyabaev, Methanol synthesis from the catalytic hydrogenation of CO2 over CuO–ZnO supported on aluminum and silicon oxides, J. Taiwan Inst. Chem. Eng. 78 (2017) 416–422.
[59] W.Y. Hernández, F. Aliç, A. Verberckmoes, P. Van Der Voort, Tuning the acidic–basic properties by Zn-substitution in Mg–Al hydrotalcites as optimal catalysts for the aldol condensation reaction, J. Mater. Sci. 52 (2017) 628–642.
[60] B.R. Strohmeier, An ESCA method for determining the oxide thickness on aluminum alloys, Surf. Interface Anal. 15 (1) (1990) 51–56.
[61] M.C. Biesinger, Advanced analysis of copper X-ray photoelectron spectra, Surf. Interface Anal. 49 (13) (2017) 1325–1334.
[62] M.C. Biesinger, L.W. Lau, A.R. Gerson, R.S.C. Smart, Resolving surface chemical states in XPS analysis of first row transition metals, oxides and hydroxides: Sc, Ti, V, Cu and Zn, Appl. Surf. Sci. 257 (3) (2010) 887–898.
[63] I.S. Zhidkov, A.A. Belik, A.I. Kukharenko, S.O. Cholakh, L.S. Taran, A. Fujimori, S. V. Streltsov, E. Kurmaev, Cu-site disorder in CuAl2O4 as studied by XPS spectroscopy, JETP Lett. 114 (9) (2021) 556–560.
[64] M. Laurenti, G. Canavese, S. Stassi, M. Fontana, M. Castellino, C. Pirri, V. Cauda, A porous nanobranched structure: an effective way to improve piezoelectricity in sputtered ZnO thin films, RSC Adv. 6 (80) (2016) 76996–77004.
[65] G. Deroubaix, P. Marcus, X-ray photoelectron spectroscopy analysis of copper and zinc oxides and sulphides, Surf. Interface Anal. 18 (1) (1992) 39–46.
[66] R. Gaikwad, A. Bansode, A. Urakawa, High-pressure advantages in stoichiometric hydrogenation of carbon dioxide to methanol, J. Catal. 343 (2016) 127–132.
[67] G. Pacchioni, From CO2 to methanol on cu/ZnO/Al2O3 industrial catalyst. What do we know about the active phase and the reaction mechanism? ACS Catal. 14 (4) (2024) 2730–2745.
[68] A.L. Pinheiro, A.N. Pinheiro, A. Valentini, J. Mendes Filho, F.F. de Sousa, J.R. de Sousa, C.R. Maria da Graça, P. Bargiela, A.C. Oliveira, Analysis of coke deposition and study of the structural features of MAl2O4 catalysts for the dry reforming of methane, Catal. Commun. 11 (1) (2009) 11–14.
[69] Y. Khani, F. Bahadoran, S. Soltanali, J.S. Ahari, Hydrogen production by methanol steam reforming on a cordierite monolith reactor coated with cu–Ni/LaZnAlO 4 and Cu–Ni/γ-Al 2 O 3 catalysts, Res. Chem. Intermed. 44 (2018) 925–942.
[70] R.M. Freire, F.F. de Sousa, A.L. Pinheiro, E. Longhinotti, J. Mendes Filho, A. C. Oliveira, C.F. Paulo de Tarso, A.P. Ayala, A.C. Oliveira, Studies of catalytic activity and coke deactivation of spinel oxides during ethylbenzene dehydrogenation, Appl. Catal. Gen. 359 (1–2) (2009) 165–179.
[71] A.E. Prašnikar, A. Pavlišič, F. Ruiz-Zepeda, J. Kovač, B.J.I. Likozar, E.C. Research, Mechanisms of copper-based catalyst deactivation during CO2 reduction to methanol 58 (29) (2019) 13021–13029.
[72] N. Iwasa, H. Suzuki, M. Terashita, M. Arai, N. Takezawa, Methanol synthesis from CO 2 under atmospheric pressure over supported Pd catalysts, Catal. Lett. 96 (2004) 75–78.
[73] S. Kanuri, J.D. Vinodkumar, S.P. Datta, C. Chakraborty, S. Roy, S.A. Singh, S. Dinda, Methanol synthesis from CO2 via hydrogenation route: thermodynamics and process development with techno-economic feasibility analysis, Korean J. Chem. Eng. 40 (4) (2023) 810–823.
[74] T.C. Lin, M.A. Nolen, C.A. Farberow, S. Kwon, A. Bhan, Mechanistic and kinetic relevance of hydrogen and water in CO2 hydrogenation on Cu-based catalysts, J. Catal. 443 (2025) 115936.
[75] J. Cored, C.W. Lopes, L. Liu, J. Soriano, G. Agostini, B. Solsona, R. Sánchez-Tovar, P. Concepción, Cu-Ga3+-doped wurtzite ZnO interface as driving force for enhanced methanol production in co-precipitated Cu/ZnO/Ga2O3 catalysts, J. Catal. 407 (2022) 149–161.
[76] S. Ren, X. Fan, Z. Shang, W.R. Shoemaker, L. Ma, T. Wu, S. Li, N.B. Klinghoffer, M. Yu, X. Liang, Enhanced catalytic performance of Zr modified CuO/ZnO/Al2O3 catalyst for methanol and DME synthesis via CO2 hydrogenation, J CO_2 Util 36 (2020) 82–95.